Solid State Nuclear Magnetic Resonance 143 (2026) 102080

Contents lists available at ScienceDirect

Solid State Nuclear Magnetic Resonance

journal homepage: www.elsevier.com/locate/ssnmr

Ultra-high field solid-state NMR of microporous materials at 1 GHz and beyond: A mini review

Wanli Zhang [a,b,*], Zhehong Gan [c], Yining Huang [a,**]

[a] Department of Chemistry, The University of Western Ontario, London, Ontario, N6A 5B7, Canada
[b] Centre of High Field NMR Spectroscopy and Imaging, Nanyang Technological University, 21 Nanyang Link, Singapore, 637371, Singapore
[c] National High Magnetic Field Laboratory, 1800 E. Paul Dirac Drive, Tallahassee, FL, 32310, United States

ARTICLE INFO

Handling Editor: Olivier Lafon

ABSTRACT

Microporous materials, including zeolites and metal–organic frameworks (MOFs), play pivotal roles in a wide range of applications such as catalysis, gas adsorption/separation, drug delivery, and chemical sensing. Establishing their structure–property relationships requires detailed characterization of local structures. Solid-state nuclear magnetic resonance (NMR) spectroscopy, as an isotope- and site-specific technique, is ideally suited for probing local chemical environments at atomic level in these materials. However, many NMR-active nuclei in microporous materials are inherently unreceptive due to low gyromagnetic ratios, low natural abundances, and/or large quadrupolar interactions. The advent of ultra-high magnetic fields at 1 GHz and beyond has significantly expanded the capabilities of solid-state NMR by offering substantial gains in both sensitivity and resolution. This review summarizes recent advances in solid-state NMR studies of microporous materials enabled by ultra-high magnetic fields. We first briefly introduce the sensitivity enhancements afforded by high-field NMR and the development of ultra-high field magnet technologies. We then discuss the experimental methodologies for characterizing microporous materials at ultra-high magnetic fields. We highlight the recent multinuclear solid-state NMR studies that elucidate metal centers, organic linkers, and host–guest interactions in zeolites and MOFs at ultra-high magnetic fields. Finally, we discuss emerging opportunities and future research directions for ultra-high field solid-state NMR in the study of microporous materials.

1. Introduction

Microporous materials with pore size below *ca.* 2 nm play essential roles in modulating the behavior of confined guest molecules, enabling various applications such as gas adsorption [1], storage [2], separation [3–6], and catalysis [7,8]. This class of materials includes organic porous materials (*e.g.*, covalent organic frameworks (COFs)) [9], inorganic materials (*e.g.*, zeolites [10], porous carbon [11]), organic/inorganic hybrid materials such as metal-organic frameworks (MOFs) [12,13].

The structural characterization of microporous materials includes X-ray diffraction (XRD), X-ray absorption spectroscopy, electron microscopy (EM), thermal gravimetric analysis (TGA), adsorption–desorption isotherms, vibrational spectroscopy, solid-state nuclear magnetic resonance (NMR) *etc*. The XRD characterizes the long-range information in crystalline materials. However, high-quality single crystal is needed to accurately determine the structures, which is not always available for microporous materials. Solid-state NMR [14] is a powerful tool for probing the local environments of specific nuclei, spatial proximities, and the dynamics of guest molecules, even in disordered systems where long-range structural order is absent [14,15]. Through multinuclear detection and multidimensional correlation experiments, solid-state NMR can reveal atomic-level connectivity and spatial proximity relationships, providing structural insights that are often difficult to obtain using vibrational spectroscopies such as infrared (IR) and Raman spectroscopy.

Over the past decades, solid-state NMR has been widely applied in the characterization of microporous materials, and there are many excellent reviews and books [16–30]. In recent years, the development of ultra-high magnetic fields, including commercial Gigahertz

This article is part of a special issue entitled: ssNMR above 1 GHz and beyond published in Solid State Nuclear Magnetic Resonance.

* Corresponding author. Department of Chemistry, The University of Western Ontario, London, Ontario N6A 5B7, Canada.
** Corresponding author.
E-mail addresses: wzhan728@uwo.ca, wanli.zhang@ntu.edu.sg (W. Zhang), yhuang@uwo.ca (Y. Huang).

https://doi.org/10.1016/j.ssnmr.2026.102080
Received 28 February 2026; Received in revised form 25 March 2026; Accepted 25 March 2026
Available online 26 March 2026

superconducting NMR instruments (1.0 GHz, 23.5 T; 1.1 GHz; 25.9 T; 1.2 GHz, 28.2 T) [31,32], and the specially designed series-connected hybrid (superconducting and powered) magnet (SCH, 1.5 GHz, 35.2 T) at National High Magnetic Field Laboratory, Florida, USA [33], enable the access to many insensitive nuclei owing to large electric quadrupolar interaction, low gyromagnetic ratio, low natural abundance *etc*.

Since becoming available, these high magnetic fields have enabled dramatic improvements in the sensitivity and resolution of solid-state NMR. The 1 GHz and beyond solid-state NMR spectroscopy has been widely used in biological systems [34–36], such as membranes [37], DNA/RNA [38,39], and proteins [40–51]. In the meanwhile, the ultra-high field NMR was also employed in materials science studies, including organic compounds [52–59], organometallic compounds [60–65], metal salts [66,67], metal sulfide [68,69], metal oxide [70–76], perovskites [77], solid-state electrolytes [78], glasses [79–82], catalysts [70,71,83–85] and so on.

Herein, we review the solid-state NMR studies of microporous materials including zeolite and MOFs at GHz and beyond magnets. We outline how advanced solid-state NMR methods can address key questions related to structure, interactions, and dynamics in these materials. Current challenges and future opportunities for solid-state NMR in porous-material research are also presented.

2. Basics of ultra-high-field NMR

2.1. Sensitivity enhancement by high-field NMR

Sensitivity is one of the most critical challenges for solid-state NMR spectroscopy. The Boltzmann polarization under thermal equilibrium is relatively small, as the net magnetization M is proportional to B_0, expressed as [86]

$$M = \frac{N\gamma^2\hbar^2 I(I+1)}{3kT} B_0,$$

where N is the number of spins, γ is gyromagnetic ratio, I is the spin number, k is Boltzmann constant ($k = 1.380649 \times 10^{-23}$ J/K).

The modern NMR spectrometers apply the RF pulse to make the magnetization transverse with a 90° pulse. The induced current of the coil, *i.e.* the signal (V_{signal}) is proportional to the time derivative of magnetic flux ($\varnothing$) in the coil, expressed as [87,88]

$$V_{signal} \propto -\int \frac{\partial \varnothing}{\partial t} dv_s,$$

where v_s denotes the volume element.

For quadrupolar nuclei ($I > 1/2$), the sensitivity may suffer from quadrupolar interactions (QI) between quadrupolar moment and electric field gradient (EFG) from surroundings. The EFG tensor is described by its three principal components V_{xx}, V_{yy} and V_{zz} ($|V_{zz}| \geq |V_{yy}| \geq |V_{xx}|$). The quadrupole coupling constant is defined as $C_Q = eQV_{zz}/h$, and the asymmetry parameter is given by $\eta_Q = (V_{xx} - V_{yy})/V_{zz}$. Assuming $\eta_Q = 0$, the second-order quadrupolar interaction is expressed as [89]

$$\nu_Q^{(2)} = -\left(\frac{{\nu_Q}^2}{16\nu_0}\right)\left(I(I+1) - \frac{3}{4}\right)\left[1 - cos^2\,\theta\right]\left[9\,cos^2\,\theta - 1\right],$$

where ν_Q is quadrupolar frequency, ν_0 is Larmor frequency, θ is the angle between the largest component of EFG and static magnetic field. The orientation dependent second-order shift gives rise to the spectral broadening to the central transition of half-integer quadrupolar nuclei.

Therefore, the low sensitivity of solid-state NMR can originate from 1) low natural abundance (*i.e.*, low N, *e.g.*, ^{17}O, ^{43}Ca); 2) low gyromagnetic ratio (*e.g.*, ^{67}Zn, ^{89}Y); 3) large QI (*e.g.*, ^{209}Bi, ^{127}I); 4) large chemical shift anisotropy (*e.g.*, ^{195}Pt); 5) long spin-lattice relaxation (T_1, *e.g.*, ^{109}Ag); and a combination of these factors.

Performing solid-state NMR at higher static magnetic field enables not only a sensitivity enhancement but also reduced second order quadrupolar broadening. In addition, the larger chemical shift dispersion in frequency leads to better resolution.

2.2. Development of magnets for high-field NMR

Bruker has an extensive history in the design and manufacture of high-field NMR magnets. The first 1.0 GHz system was installed in 2009 at the European Centre for High Field NMR (CRMN) in Lyon [90]. The magnet was built with niobium-titanium (NbTi) and 15% bronze niobium-tin (Nb_3Sn) superconductors [32]. In 2015, a 1020 MHz NMR was built in National Institute for Materials Science (NIMS) by JEOL, RIKEN, and NIMS [91]. The magnet consists of low-T_c superconductors (LTS) NbTi and Nb_3Sn and a high-T_c superconductor (HTS), Bi-2223 [91]. Afterwards in 2018, the world's first fully superconducting, persistent 1.1 GHz NMR magnet was developed at Bruker's UHF facility in Switzerland. And the world's first 1.2 GHz all-superconducting NMR spectrometer was installed in 'Centro Risonanze Magnetiche' (CERM) of the University of Florence in Italy in 2020 [92,93]. The 1.2 GHz NMR magnet used an HTS/LTS hybrid design with NbTi, Nb_3Sn and ReBCO conductors [32]. Recently, Bruker has announced the successful development of the world's first high-resolution 1.3 GHz NMR spectrometer with a stable, standard-bore 54 mm superconducting magnet in the Joint ENC-ISMAR Conference 2025 [94].

Besides the development of superconducting magnet for NMR, the series-connected hybrid (SCH) magnet up to 36 T ($\nu_0(^1H) = 1.5$ GHz) was developed at National High Magnetic Field Laboratory, Tallahassee in 2017 [33]. The SCH magnet consists of a resistive insert and superconducting outsert with their coils connected in series. The large inductance superconducting outsert coil helps damping the fluctuation of the field generated by the resistive inner coils. As the resistive and superconducting sections operate in series, the current through the superconducting magnet must be ramped together with the resistive magnet. The superconducting coil is built with a cable-in-conduit conductor (CICC) design, where Nb_3Sn wires are bundled within a stainless-steel pipe capable of carrying current up to 20 kilo amp. Supercritical helium circulates through *ca.* 30% internal void space of the CICC to maintain the Nb_3Sn in superconducting state and to dissipate the heat from conventional conductor of the conduit. The SCH design allows the ramping the magnet to its full 36 T field in *ca.* 30 min [95]. All the NMR probes for SCH is equipped with a magnetic flux pickup coil and ^{7}Li NMR field-frequency lock circuitry to suppress fast and slow fluctuating field components, respectively, using a home-developed regulation system. A 6.84 M LiCl aqueous solution doped with 750 mM $MnCl_2$ was used to provide a strong and fast responding ^{7}Li NMR signal for lock purpose [33]. To date, the 36 T SCH magnet has supported hundreds of studies, ranging from biological applications to materials science [52,60,61,66,69,71,78].

2.3. Solid-state NMR methods

2.3.1. High resolution solid-state NMR

The standard NMR technique for averaging anisotropic interactions (*e.g.*, dipolar interaction, chemical shift anisotropy) is magic angle spinning (MAS) [96]. The sample is rotating around an axis at 54.736° with respect to static magnetic field B_0, from 5 kHz to 200 kHz [97]. In recent years, ultrafast MAS, with spinning rates above 100 kHz, has emerged as a powerful approach in solid-state NMR spectroscopy [97]. Such high spinning rates substantially improve spectral resolution by efficiently suppressing strong homonuclear dipolar couplings, particularly among ^{1}H nuclei in proton-rich systems such as proteins [97–100]. In addition, fast MAS enables the acquisition of high-resolution NMR spectra for nuclei exhibiting very broad lineshapes under stationary conditions, such as ^{14}N [101,102].

Under MAS, both homonuclear/heteronuclear correlation can be

investigated using high-resolution solid-state NMR spectroscopy. The widely used techniques in characterizing microporous materials include double-quantum single-quantum (DQ-SQ) [103], heteronuclear correlation (HETCOR), J-mediated heteronuclear multiple-quantum coherence (J-HMQC) [104], dipolar heteronuclear multiple-quantum coherence (D-HMQC) [105], transfer of populations double resonance (TRAPDOR) [106], rotational echo double resonance (REDOR) [107], rotational echo adiabatic passage double resonance (REAPDOR) [108], resonance-echo saturation-pulse double-resonance (RESPDOR) [109], *etc*. Among these methods, DQ-SQ and spin exchange experiments are widely used homonuclear correlation techniques for probing spatial proximities between identical nuclei. DQ–SQ correlations originate from the excitation and reconversion of double-quantum coherences mediated by homonuclear dipolar couplings, whereas spin exchange experiments probe magnetization exchange between nearby spins during a mixing period. Although the resulting two-dimensional spectra may appear visually similar, the underlying physical mechanisms and spectral interpretations are fundamentally different. An important experiment for half-integer quadrupolar nuclei is the multiple-quantum MAS (MQMAS) [110] capable of averaging out the second-order quadrupolar broadening. In this review, we briefly describe DQMAS, MQMAS and D-HMQC, which are commonly utilized in high-field solid-state NMR characterization of microporous materials.

2.3.1.1. Double-Quantum (DQ) MAS. The nuclei studied in DQMAS include both spin-1/2 and quadrupolar nuclei to observe the two-spin coherences of a homonuclear spin pair. For spin-1/2 spins, a single nucleus only has a single-quantum transition. Any DQ NMR signals are definitely from spin pairs coupled by the homonuclear dipolar interaction [103]. Under MAS, the dipolar coupling needs be reintroduced using multiple-pulse sequence often called dipolar recoupling [111]. The most commonly used DQ homonuclear recoupling sequence for nuclei with small chemical shift anisotropy such as protons is Back to Back (BABA) [112,113], which are used during both excitation and conversion periods (Fig. 1(a)). For BABA DQ MAS, rotor-synchronization is always required. DQ coherence between two equivalent spins (AA or BB) produces a single self-correlation peak located on the diagonal of the spectrum. In contrast, DQ coherence between two non-equivalent spins (AB) gives rise to a pair of cross peaks with equal intensity, symmetrically positioned about the diagonal. In practice, DQ–SQ correlation experiments often employ symmetry-based dipolar recoupling sequences [114], such as POST-C7 [115] and $R12_5^2$ [114,116], to enhance the excitation and reconversion efficiencies of double-quantum coherences under magic-angle spinning conditions.

Dipolar recoupling is necessary for generating two-spin DQ coherence between a pair of quadrupolar nuclei based on spatial proximity under MAS. For half-integer quadrupolar nuclei, there are more two energy levels for the central transition. Strong *rf* pulses can cause coherence loss from the central to other transitions such as satellite and multiple-quantum transitions. Recoupling pulse sequences with lower to moderate rf field can reduce these losses for better efficiencies. A commonly used $BR2_2^1$ sequence using symmetry-based recoupling scheme [117] spans four rotor periods for DQ excitation/conversion is shown in Fig. 1(b). In addition, DQ coherence within a single spin of quadrupolar nuclei can also exist mixing with the desired two-spin DQ coherence. Separation of the two-type DQ coherences can be achieved by applying a CT-selective π-pulse during the evolution period and phase cycling for filtering out undesired single-spin DQ signals [117]. In Fig. 1 (b), the time delays flanking the CT-selective π-pulse are two asymmetrically incremented intervals, denoted as qt_1 and $(1-q)t_1$ [118]. By adjusting the q values, the observed CT DQ coherence frequency in indirect dimension is scaled by $(1-2q)(\omega_j+\omega_k)$, where ω_j and ω_k correspond to the CT SQ resonant frequencies of the two interacting spins [117]. Considering the weak RF field strengths in $BR2_2^1$ recoupling scheme, the DQ excitation efficiency is also greatly affected by the offset to the carrier frequency [71]. Thus, the correlation signals may be weakened due to insufficient excitation on desired chemical shift range, especially at high magnetic fields [71]. There is an excellent review on using ^{27}Al-^{27}Al DQ MAS NMR in the characterization of microporous materials [119].

2.3.1.2. Multiple Quantum (MQ) MAS. In MAS solid-state NMR, the QI between the quadrupolar nuclei ($I > 1/2$) and the EFG induces anisotropic broadening. The signal from the satellite transitions usually consists of many spinning sidebands with low intensity because the first-order quadrupolar interaction is usually orders of magnitude larger than

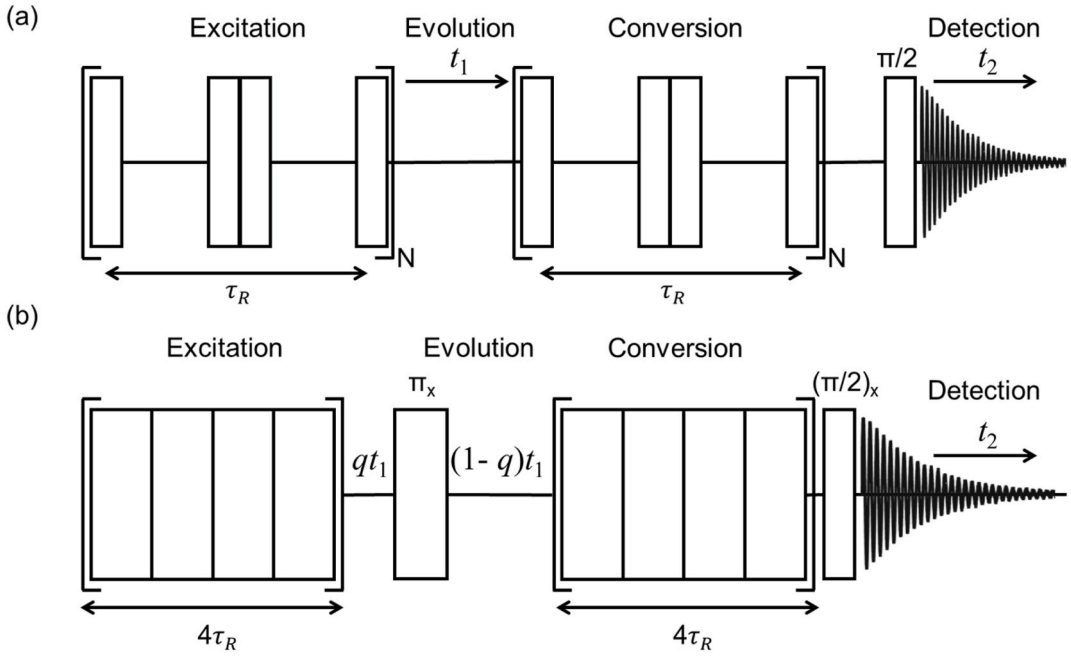

Fig. 1. (a) Pulse sequence of BABA-1 DQ-SQ MAS experiment. The excitation/conversion covers multiple times of rotor period. (b) DQ-SQ pulse sequence using $BR2_2^1$ recoupling scheme [117].

the MAS spinning rate. In contrast, the central transition (CT) is free from the first-order QI, thus broadened only by the much smaller second-order effects. NMR spectra of half-integer quadrupolar nuclei is usually dominated by the signal from the central transition [89]. However, the second-order interaction contains anisotropic terms $Y_{lm}(\theta,\varphi)$ up to the fourth $l=4$ rank. Only the second-rank term, scaled by $P_2(\cos\theta_{MAS})$, is averaged out under MAS in the same way of chemical shift anisotropy of spin-1/2 [89]. The remaining $Y_{4m}(\theta,\varphi)$ terms scaled by MAS lead to anisotropic broadening to MAS spectra of half-integer quadrupolar nuclei together with the isotropic $l=0$ shift. Because second-order quadrupolar broadening is inversely proportional to the main magnetic field B_0, ultrahigh-field solid-state NMR offers a major advantage for studying quadrupolar nuclei.

Two-dimensional MQMAS experiment which correlates the MQ transition (coherence between spin energy levels $M/2$ and $-M/2$) with the single-quantum CT is capable to remove all anisotropic broadening in the form of a two-dimensional experiment [110]. It has become a powerful and widely used experiment achieving high isotropic resolution of half-integer quadrupolar nuclei without anisotropic broadening. The simplest 3QMAS pulse sequence consists of two pulses [110]. However, the two coherence transfer pathways (0Q → +3Q → -1Q and 0Q → −3Q → −1Q) are asymmetric and generally exhibit unequal efficiencies. In order to acquire absorptive phased 2D spectra, a third π/2 soft pulse is added with a z-filter making the two coherence transfer pathways (0Q → ±3Q →0Q → -1Q) symmetric with equal intensity for pure adsorption lineshape [120]. Absorptive lineshape can also be obtained with signal from just one pathway, −3Q → −1Q for spin $I=3/2$ or +3Q → −1Q for $I>3/2$. A full phase modulated echo using a π soft pulse yields absorptive lineshape of the 2D spectra [121]. The shifted-echo MQMAS sequence is often used for samples with large quadrupolar broadening and long T_2 such that untruncated full echo signals are acquired for all sites. Numerous pulse schemes have been developed to enhance the multiple-quantum excitation and conversion efficiency. Recently, it has also been shown that cosine modulated pulses lasting one rotor period long selective to satellite transitions (STs) convert efficiently between central and MQ coherences. The cosine low-power MQMAS is particularly useful for samples with large QIs [122].

2.3.1.3. D-HMQC. The dipolar based D-HMQC NMR has been developed for hetero-correlation (HETCOR) with quadrupolar nuclei [105,123,124]. The HMQC sequence employs two pulses to encode the nucleus observed indirectly. The short pulses make HMQC suitable to cover wide bandwidth and was first used for detecting integer spin-1 ^{14}N nuclei indirectly via ^{13}C [125]. The HMQC sequence was soon adapted to half-integer nuclei [126]. Compared to the other commonly used method with cross-polarization, HMQC avoids the spin-lock of quadrupolar nuclei under MAS because the level crossings of *rf* with satellite transitions under MAS causes leaks of polarization from central transition [127]. The heteronuclear two-spin coherence can be generated with dipolar recoupling such as R^3 [125], symmetry-based sequences [128], REDOR [107] and simultaneous frequency and amplitude modulation (SFAM) [129,130]. For proton-detected D-HMQC, the $SR4_1^2$ recoupling scheme is usually used under fast MAS [123]. As mentioned above, applying multiple pulses to central transition of half-integer quadrupolar nuclei can cause polarization losses to other transitions, the recoupling pulses are usually preferred to be applied on the spin-1/2 nuclei, either in direct dimension or indirect dimension (Fig. 2) [131]. The latter "indirect recoupling" scheme is more robust to rotor synchronization in terms of t_1-noise [105]' [132]. For the former "direct recoupling", a modified pulse sequence termed t_1-noise eliminated (TONE) D-HMQC was proposed to reduce the t_1 noise by introducing ^{1}H π refocusing pulses [133]. Recently, Hung *et al.* demonstrated that under very fast MAS, regions of *rf* fields can be found with good spin-lock and matching the Hartmann-Hahn condition modified by the MAS for cross-polarization. Because ^{1}H spin lock usually lasts longer than the spin-echo in HMQC, the double cross-polarization (DCP) method provides visible signal enhancement over HMQC under the ultra-fast MAS [134]. In addition to correlations between spin-1/2 and quadrupolar nuclei, D-HMQC type experiments have also been applied to probe heteronuclear correlations between two half-integer quadrupolar nuclei. Such approaches enable the investigation of structural connectivities between quadrupolar sites in inorganic materials, such as ^{23}Na-^{27}Al [135,136], ^{11}B-^{27}Al [137], ^{11}B-^{17}O [138], ^{27}Al-^{17}O [139].

2.3.2. Wideline solid-state NMR

In many solid-state NMR experiments, the anisotropic broadening of NMR spectra is so large that the powder pattern features breadth from 250 kHz to tens of MHz [140]. The current MAS techniques cannot always effectively remove such large anisotropic broadening so that many NMR experiments are performed under stationary conditions. Carr--Purcell Meiboom-Gill (CPMG) pulse sequence refocused the rapid-decaying signal repetitively generating a long echo train which effectively enhances signal-to-noise by coadding the echoes or direct Fourier transformation of the echo train signal. The latter generates a spectrum of spikelets with their intensity envelope matching the powder lineshape [140–142]. Furthermore in case that CPMG with a single frequency is not sufficient to the breadth of powder lineshape over MHz, the variable-offset cumulative spectrum (VOCS) method is necessary for mapping out the whole pattern [143]. In this subsection, the basic methods including CPMG and VOCS will be briefly introduced.

2.3.2.1. CPMG. There are several pulse sequences for acquisition of UW NMR spectra. The large anisotropic interaction (the QI and/or CSA, and/or hyperfine interaction) usually leads to rapid transverse (T_2) and effective transverse (T_2*) relaxation. Acquiring Bloch decay using a

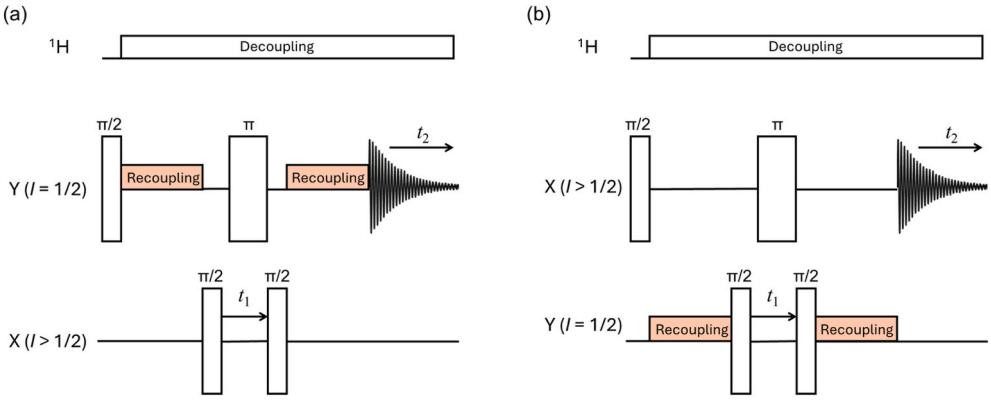

Fig. 2. Pulse sequences of the (a) Y{X} D-HMQC and (b) X{Y} D-HMQC NMR experiments.

single-pulse experiment often yield distorted lineshapes as the transmit/receive (T/R) switch dead time prevents the acquisition at the beginning of the FID. Probe ringing especially at low resonance frequencies tends to corrupt the FID immediately after the π/2 pulse. A standard Hahn-echo experiment (Fig. 3(a)) is necessary to refocus the large and inhomogeneous broadening [144]. As the T_2 relaxation rates of quadrupolar nuclei is typically longer than T_2*, the signal-to-noise (SNR) can be enhanced through strategies of Carr-Purcell-Meiboom-Gill (CPMG) trains after the initial excitation (Fig. 3(b)). The Fourier transformation of an echo train yields a spectrum of series of sharp "spikelets" in frequency domain, where the spikelet frequency equals to the inverse of echo spacing in time-domain. i.e. 1/(echo size in points × dwell) [145–147]. In the CPMG pulse sequence (Fig. 3(b)), the rectangular-shaped pulses are used to excite and refocus the magnetization. Refocusing pulses shorter than 180° can be used to increase the frequency bandwidth. A rectangular pulse τ has a frequency profile of sinc function with a node 1/τ [146]. To achieve broader and more uniform excitation bandwidth, adiabatic wideband uniform-rate smooth truncation (WURST) pulses can be employed [146,148]. The WURST-CPMG sequence (Fig. 3(c)) has been applied to acquire UW NMR spectra of both spin-1/2 and quadrupolar nuclei [149–151]. It should be noted that identical WURST pulses are usually used for the excitation and refocusing. Also, magnitude spectra are often used after Fourier transformation because the phasing of spectra acquired using WURST requires second-order adjustment [146,152]. Furthermore, the WURST pulse is frequency swept and lasts for relatively longer duration (tens of μs) than hard pulses, it is not advantageous when T_2 is short. Hansen *et al.* has reported an ultrafast frequency-swept pulse to partially mitigate this challenge, especially useful in characterizing paramagnetic solids with short homogeneous transverse relaxation times [153].

2.3.2.2. VOCS. Even with broadband pulses, the breadth of UW NMR spectra can also beyond the excitation bandwidth in one spectral window. To acquire powder pattern beyond MHz, the variable-offset cumulative spectrum (VOCS) approach is necessary [143]. For superconducting magnets with fixed fields, one approach is to acquire multiple individual spectra with transmitter stepping equal frequency steps (Fig. 4(a)). The undistorted UW NMR spectrum is constructed from the skyline projection of the "frequency-stepped" subspectra. With this method, the probe needs to be retuned during the acquisition, and automation of the tuning has also been available [154]. The other approach is to sweep the magnetic field with fixed transmitter frequency (Fig. 4(b)) [95]. This field stepped method can be easily implemented with powered 25 T magnet [155], and the 36 T SCH magnet at the NHMFL without the need of retuning the probe [95]. Note that these two methods are equivalent only in the first-order QI and CSA. Significant deviation can be observed for ultra wide cases due to the field dependences of the second-order quadrupolar coupling and CSA [95]. It is necessary to consider the field-dependent interactions in the analysis of

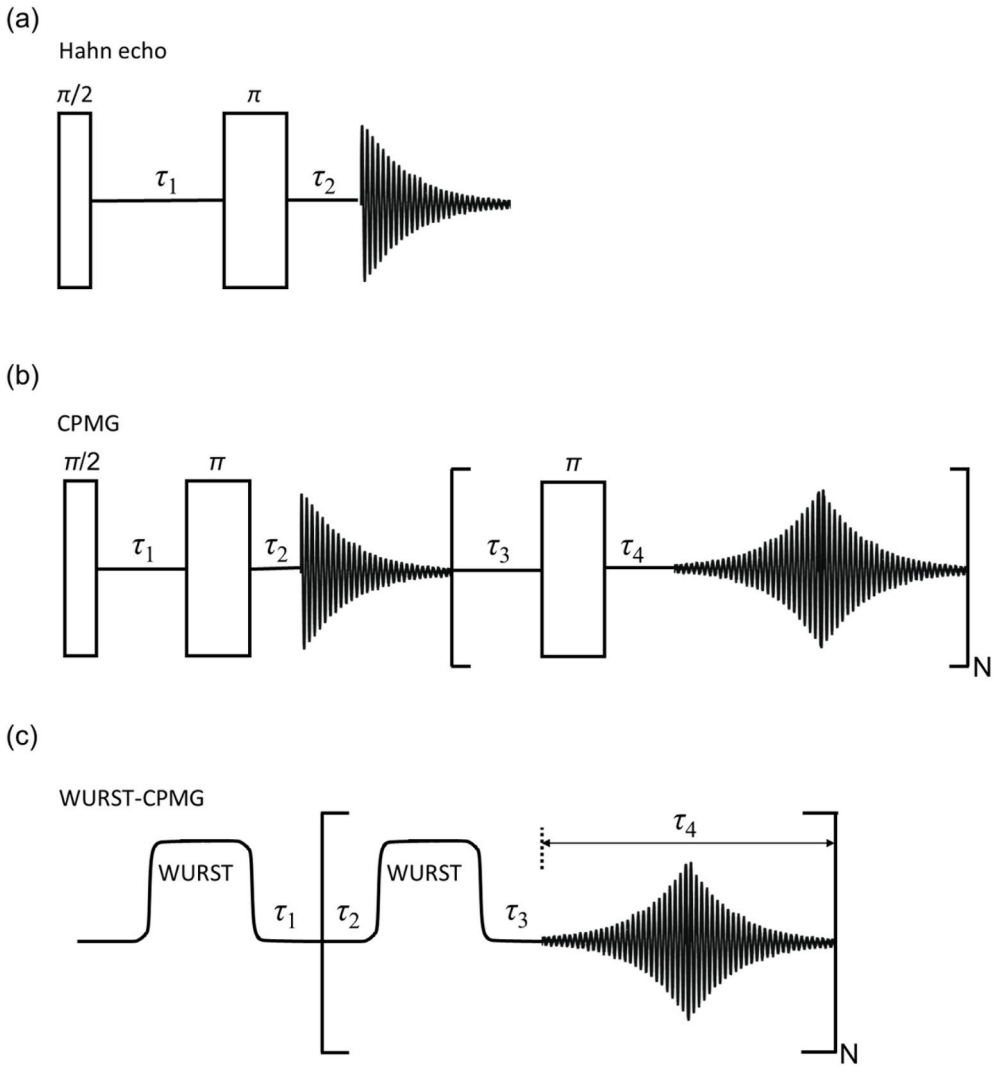

Fig. 3. The pulse sequences used to acquire UW NMR spectra.

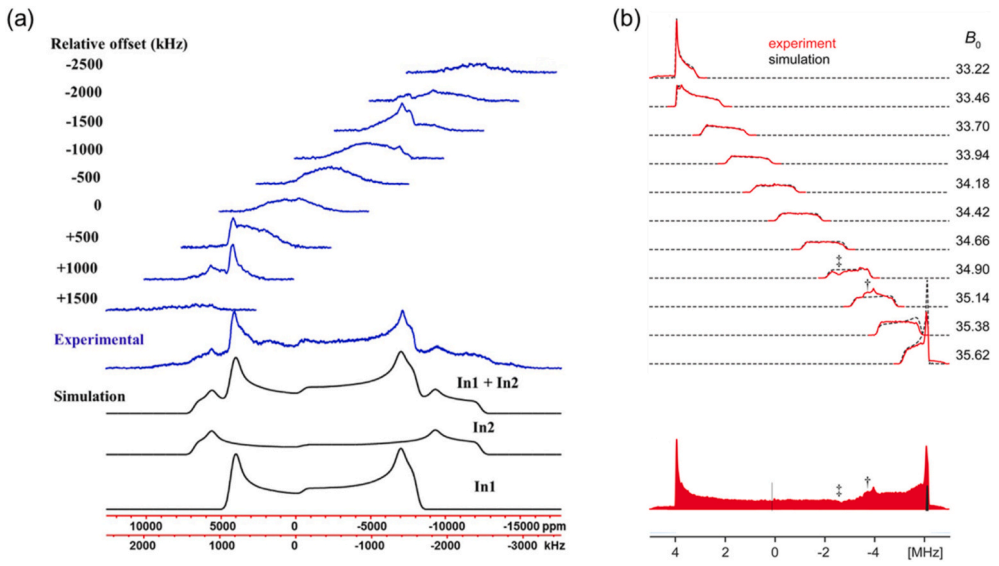

Fig. 4. Schematic illustration of the VOCS methods. (a) Frequency-stepping approach was used to acquire the static ^{115}In NMR spectrum of MIL-68(In) MOF at 21.1 T. Nine subspectra were collected with a step of 500 kHz. The individual sub-spectra (top) are summed to reconstruct the powder pattern at the bottom. Reproduced with permission from Ref. [156] Copyright 2014 Elsevier. (b) Field-stepping approach was used to acquire the ^{35}Cl static NMR spectrum of N-chlorosuccinimide. The magnetic field is changed with a step corresponding to Larmor frequency $\Delta\nu_0(^{35}\mathrm{Cl})$ of ±1.0 MHz. Reproduced with permission from Ref. [95]. Copyright 2020 Wiley-VCH.

UW NMR acquired with field-stepping approach to determine reliable quadrupolar coupling and CSA parameters. The choices of spin echo, CPMG, and WURST-CPMG pulse sequences depends on the span of the powder pattern, T_2 relaxation and the accesses of powered magnets between the frequency-stepping or field-stepping strategy for the acquisition of UW NMR spectra.

3. Recent advances of solid-state NMR of microporous materials at 1 GHz and beyond

3.1. Ultra-high field NMR of zeolites

Zeolites are a class of inorganic crystalline porous materials, widely used in catalysis, ion exchange, and separation processes [10]. Their classical aluminosilicate frameworks consist of three-dimensional, four-connected TO_4 (T = Si, Al) tetrahedra, which can be probed by ^{27}Al, ^{29}Si, and ^{17}O NMR spectroscopy [28,29]. Loading guest ions has proven to be an effective strategy for introducing additional active sites, thereby enhancing the catalytic performance of zeolites [157]. The characterization of the guest active sites is challenging due to their very low concentrations. Using ultra-high magnetic field provides opportunity to achieve atomic level characterization of the guest ions in zeolites [158].

3.1.1. ^{27}Al, ^{29}Si, ^{17}O NMR of zeolites

^{27}Al is a quadrupolar nucleus ($I = 5/2$) and experiences moderate QI ($Q = 146.6$ mb) [159,160]. Higher magnetic fields significantly reduce second-order quadrupolar broadening. For example, Fig. 5 shows the static ^{27}Al 1D NMR of zeolite HZSM-5 acquired at 7.05, 9.4, 14.1, 19.6 and 35.2 T [161]. A pronounced reduction in second-order QI–dominated line broadening is observed with increasing magnetic field strength [161].

The Al sites in zeolite, which can form Brønsted acid sites, are known to serve as catalytically active sites for many reactions [162]. Resolving the different types of Al sites is important to understanding the catalytical activities. Chen *et al.* employed ^{27}Al NMR at 35.2 T to discover two distinctive framework Al(IV) sites in zeolite as Brønsted sites [163]. As shown in Fig. 6, the ^{27}Al{^{1}H} D-HMQC spectra of dehydrated HZSM-5 acquired at 35.2 T reveal two distinct tetrahedral Al sites at 51 and 54

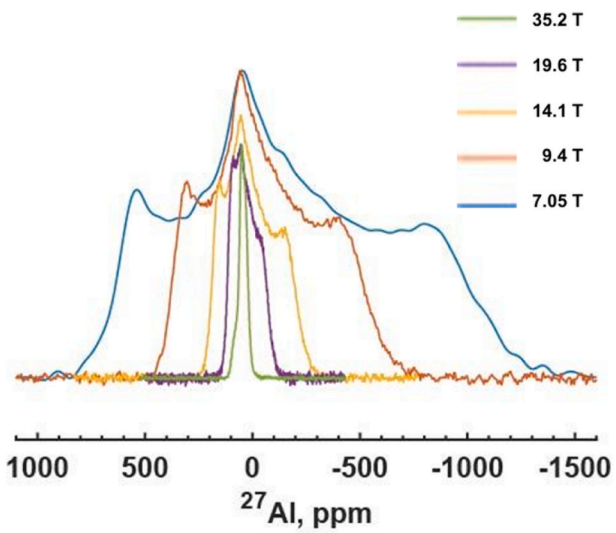

Fig. 5. Static ^{27}Al 1D NMR spectra of dehydrated HZSM-5 (Si/Al = 15) collected at 7.05, 9.4, 14.1, 19.6, and 35.2 T [161]. The H-ZSM-5 sample was dehydrated at 723 K under vacuum [161]. Reproduced with permission from Ref. [161]. Copyright 2021 American Chemical Society.

ppm, each dipolar-coupled to different protons at 4.2 and 2.8 ppm. The greatly enhanced resolution at ultra-high field, along with the distinct linewidths of the Al slices, confirms that these two Al environments are genuinely different. Note that the scale of inset 1D NMR spectra at 35.2 T covers a smaller chemical shift range than that in the spectra at 14.1 T.

During post-synthesis treatment of zeolites, the local chemical environment of the Al sites often undergoes subtle changes. Reddy *et al.* studied the structural transformation of Al sites in zeolites under hydrothermal conditions using ^{27}Al NMR at 28.2 T [164]. In pristine HY zeolites, strong 2D correlations between all framework Al environments (Al^{IV}, Al^{V}, Al^{VI}) and protons near 5 ppm reflect water molecules interacting with diverse surface Al sites (Fig. 7(b)). After hydrothermal treatment, peak shifts and the emergence of new Al^{IV} -H correlations (shaded zone in Fig. 7(c)) were observed that indicate the formation of

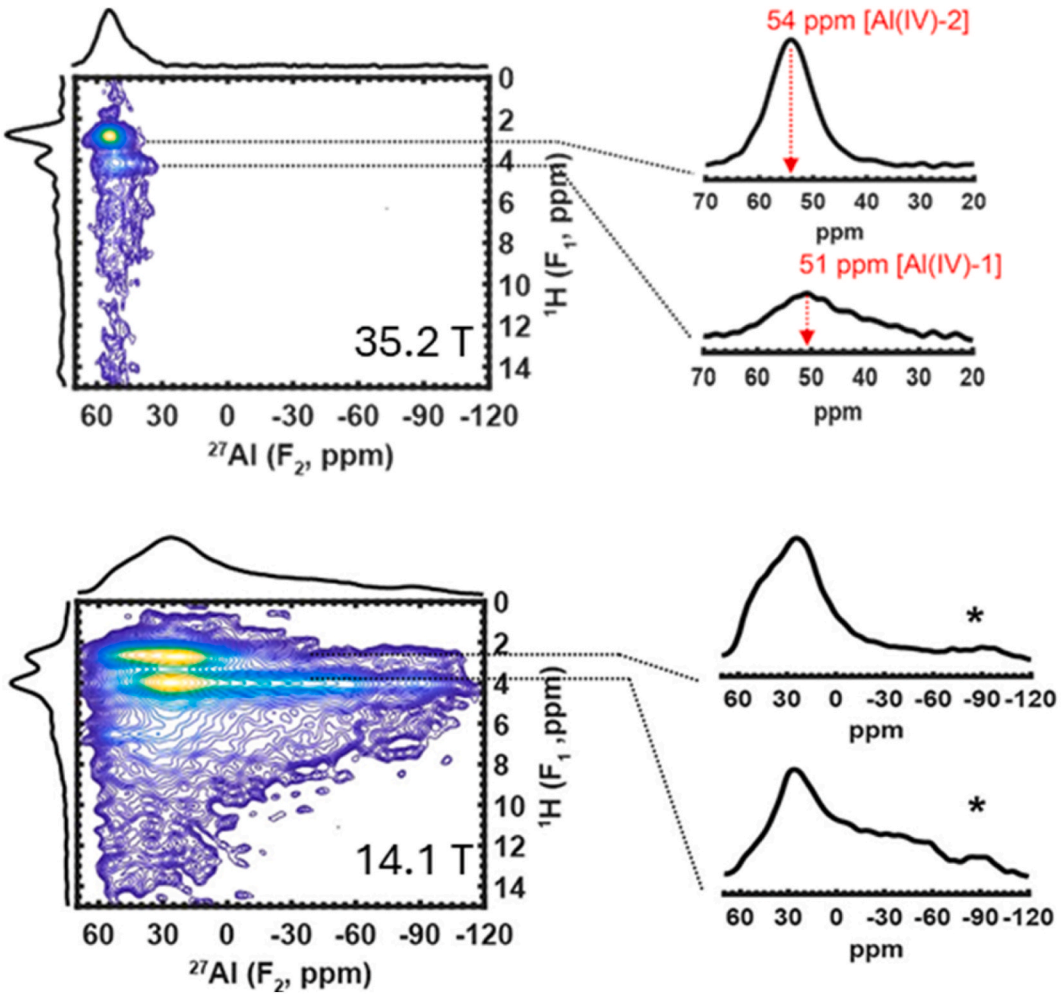

Fig. 6. 2D^{27}Al{^{1}H} D-HMQC MAS NMR spectra of dehydrated HZSM-5 catalysts acquired at magnetic fields of (Top) 35.2 T and (Bottom) 14.1 T. Reproduced with permission from Ref. [163]. Copyright 2020 American Chemical Society.

additional framework and extraframework Al (EFAl) environments. The ^{1}H spin-diffusion (SD) 2D NMR spectrum (Fig. 7(d)) before hydrothermal treatment shows four distinct resonances at 1.3, 1.7, 2.8, and 6.8 ppm, corresponding to Al–OH groups from extra-framework Al species in the sodalite cage, nonacidic silanol moieties, EFAl–OH species in the faujasite cage, and water adsorbed on Lewis acid sites, respectively [164]. After treatment, an off-diagonal peak observed between 4.8 and 9.4 ppm (Fig. 7(e)) may indicate a close spatial proximity between framework Al sites and extra-framework Al species, potentially mediated by bridging water molecules. Fan *et al.* investigated the ammonia treatment of Y zeolite (Fig. 7(f)) using ^{27}Al{^{1}H} D-HMQC at 23.5 T [165]. Y-MWNH3-0.1-30 (Y zeolite after 0.1 M NH_4OH treatment with 30 min microwave irradiation at 65 °C) shows similar ^{1}H–^{27}Al correlations to Y-MWAC, but with weaker cross peaks between Al(IV) and hydrogen with higher chemical shift and clearer ^{1}H signals associated with Al(VI)-i at 4 ppm, reflecting fewer EFAl–framework interactions [165]. The absence of correlations for the abundant Al(VI)-ii species at 0 ppm indicates highly dynamic $[Al(H_2O)_6]^{3+}$ complexes stabilized in sodalite cages. These two studies demonstrate that high field ^{27}Al NMR enables enough resolution to unravel the Al site changes during catalytic hydrothermal and ammonia treatment processes.

With the aid of ultra-high magnetic field, the resolution of ^{27}Al MQMAS NMR of zeolite can also be improved. Koller *et al.* characterized the different Al species in ion exchanged zeolite Al-SSZ-82, prepared by postsynthesis exchange of B by Al [166]. As shown in Fig. 8, the ^{27}Al 3QMAS NMR spectra acquired at 28.2 T exhibit remarkedly enhanced resolution compared to those obtained at 9.4 T, where only two signals (T10 and T11) were distinguishable. At 28.2 T, at least four distinct signals are resolved, tentatively assigned to T11, T5, T10 and T4/3 in Al-SSZ-82 [166].

Besides ^{27}Al NMR, ^{17}O NMR at high field was also used to characterize zeolites [167]. Ashbrook *et al.* investigated the structure of IPC-2P, an intermediate phase formed during zeolite structural evolution via the assembly–disassembly–organization–reassembly (ADOR) pathway [168]. Fig. 9 shows that simple incipient wetness enables isotopic exchange between framework oxygen and ^{17}O-labeled water, producing both Si–^{17}O–Si and Si–^{17}OH species [168]. The ^{17}O MQMAS NMR at both 14.1 T and 23.5 T yield two well resolved ^{17}O NMR signals ($\delta_1 \approx$ 26–35 ppm (Si–^{17}O–Si) and $\delta_1 \approx$ 16–23 ppm (Si–^{17}OH) at 14.1 T). The ^{17}O NMR spectra at F2 dimension (MAS dimension) shows greatly reduced linewidth due to reduced second order QI. The framework ^{17}O-enrichment observed in the incipient wetness experiments clarifies the bond-lability processes occurring in the ADOR intermediate [168].

3.1.2. *Characterization of guest ions in zeolites*

In addition to the zeolite frameworks, ultra-high field NMR also enables the characterization of introduced guest metal centers [158]. J. Xu *et al.* used ^{95}Mo NMR at 35.2 T to characterize the Mo-loaded ZSM-5 [169]. Mo has two NMR active nuclei, ^{95}Mo and ^{97}Mo, both of which are quadrupolar (I = 5/2). Due to the low-γ nature ($\gamma(^{95}Mo) = -1.751 \times 10^7$ rad T^{-1} s^{-1} and $\gamma(^{97}Mo) = -1.78 \times 10^7$ rad T^{-1} s^{-1}) [170], the sensitivity of the two nuclei is very low. ^{95}Mo is more preferable in NMR

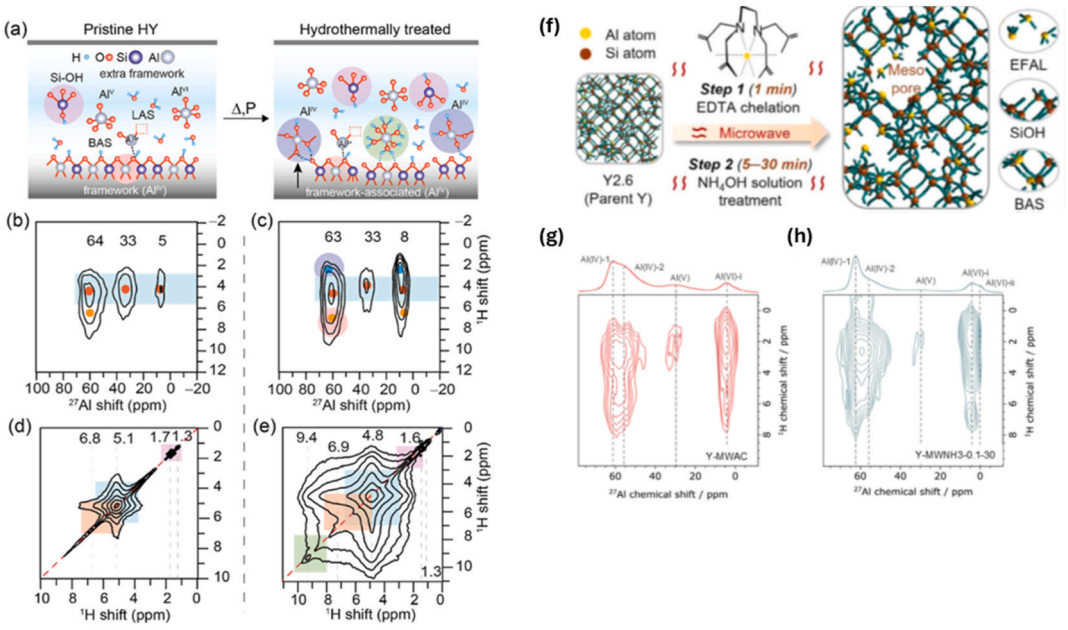

Fig. 7. (a) Schematic illustration of the structural transformations induced by hydrothermal treatment. Solid-state 2D ^{27}Al{^{1}H} D-HMQC spectra of HY zeolite (b) before and (c) after hydrothermal treatment using a recoupling time of 500 μs at 28.2 T. The 2D ^{1}H SQ-SQ spectra of HY were acquired (d) before and (e) after hydrothermal treatment with a mixing time of 100 ms at 28.2 T. The MAS spinning rate is 20 kHz for (b,c) and 55–60 kHz for (d,e). (f) Schematic illustration of the post-synthetic NH_3 treatment strategy, and ^{27}Al–^{1}H D-HMQC spectra of (g) Y-MWAC and (h) Y-MWNH_3-0.1–30. (a-e) Reproduced with permission from Ref. [164]. Copyright 2024 American Chemical Society. (f-h) Adapted with permission from Ref. [165]. Copyright 2025 Wiley-VCH.

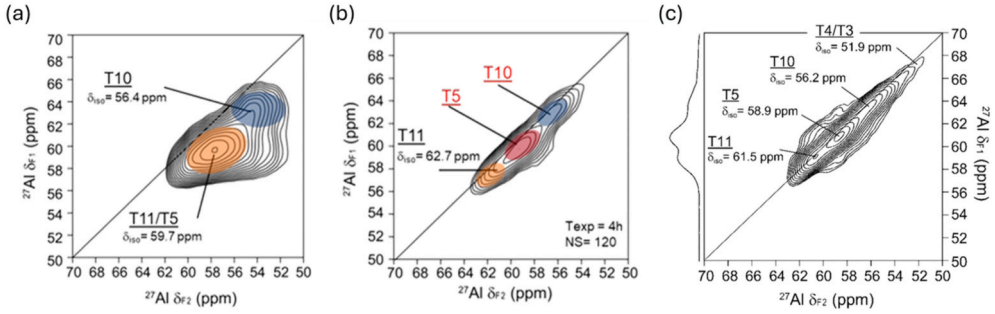

Fig. 8. ^{27}Al MQMAS NMR spectra of Al-SSZ-82$_{exchanged}$ at (a) 9.4 T and (b) 20.0 T (ν_R = 25 kHz) and (c) 28.2 T (ν_R = 50 kHz). Reproduced with permission from Ref. [166]. Copyright 2024 American Chemical Society.

experiments due to its slightly higher natural abundance (NA (^{95}Mo) = 15.92%, NA (^{97}Mo) = 9.55%) [170]. The relatively low loading level (1%-10%) of the Mo ions in ZSM-5 also leads to low isotopic concentrations, further making the acquisition of ^{95}Mo and ^{97}Mo NMR very challenging. At 35.2 T, the WURST-QCPMG MAS NMR spectrum of ZSM-5 doped with 5% Mo can be successfully acquired (Fig. 10). The spectrum was simulated with CS and EFG parameters: $\delta_{iso} \approx -35$ ppm, $C_Q \approx 5.5$ MHz, $\eta_Q = 0.7$–1.0, assigned as a MoO_3^- like local structure [171]. After 60 min of methane dehydromatization (MDA) reaction, an additional extremely broad ^{95}Mo resonance emerges ($\delta_{iso} \approx 800$ ppm, $C_Q \approx 32$ MHz, $\eta_Q = 0.9$) [170]. Although the exact Mo configuration is not determined, this demonstrates the strong interactions of the active Mo species with the anchoring BAS, yielding large C_Q values.

3.2. Ultra-high field NMR of metal-organic frameworks

3.2.1. Characterization of metal centers

Metal centers are crucial to MOF functionalities including adsorption, catalysis, drug delivery, sensing, and luminescence [172]. Understanding the impact of metal centers on the performance requires knowledge of their local coordination environments. Solid-state NMR is a powerful tool to directly access the local structures around metal centers [18,30]. With the advances of high field NMR, many unreceptive metal ions across the periodic table become accessible, such as ^{25}Mg [78,173], ^{43}Ca [174–176], $^{47/49}$Ti [177,178], ^{59}Co [179,180], $^{63/65}$Cu [179,180], ^{67}Zn [68,181] ^{73}Ge [182,183] ^{87}Sr [176,184], ^{91}Zr, [185–188], ^{93}Nb [189,190], $^{95/97}$Mo [191–193], $^{99/101}$Ru [62,194], ^{103}Rh [61,194], $^{113/115}$In Refs. [195,196], $^{135/137}$Ba [197,198], $^{185/187}$Re [60,199], ^{209}Bi [77,195,200], ^{183}W [193,201] *etc.*

Zinc exists widely in MOFs and ^{67}Zn is the only NMR active isotope. ^{67}Zn solid-state NMR is experimentally very challenging ($I = 5/2$, Q = 150 mb, N.A. = 4.1%) [159,202]. Sen and Yue *et al.* characterized the local environment of zinc in MOF glasses with the ^{67}Zn MAS NMR at 19.5 T and 35.2 T [13]. By simulating the 1D ^{67}Zn NMR at two fields (Fig. 11(a–f)), they obtained the NMR parameters (δ_{iso}, C_Q and η_Q) of the two sites in MOF ZIF-4, ZIF-zni and ZIF-62 crystals [13]. After crystalline-glass transformation, the ^{67}Zn MAS NMR spectra of ZIF-4 and ZIF-62 glasses at 19.5 and 35.2 T (Fig. 11(g) and (h)) exhibit asymmetric line shapes with low-frequency tails, reflecting a broad distribution of C_Q values arising from glassy structural disorder. The spectra are well reproduced using δ_{iso} values (277–278 ppm, close to those of the crystalline phases, 288–297 ppm) and a Czjzek distribution of C_Q, giving

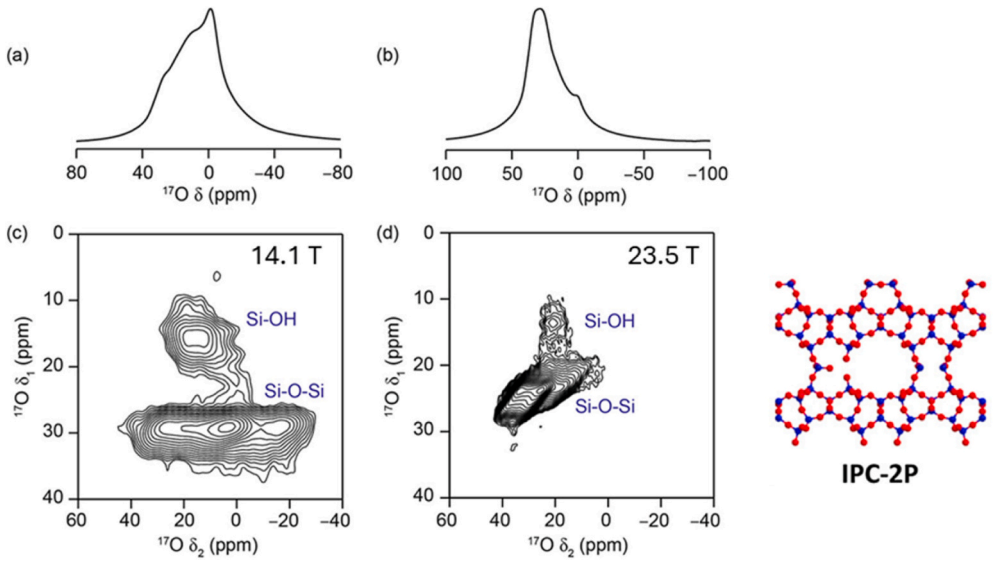

Fig. 9. Quantitative short–flip-angle (a,b) and proton-decoupled MQMAS (c,d) ^{17}O NMR spectra of ^{17}O-enriched IPC-2P ($H_2^{17}O$ incipient-wetness method), acquired at (a,c) 14.1 T (ν_r = 14 kHz) MAS and (b,d) 23.5 T (ν_r = 20 kHz) [168]. Reproduced with permission from Ref. [168]. Copyright 2023 American Chemical Society.

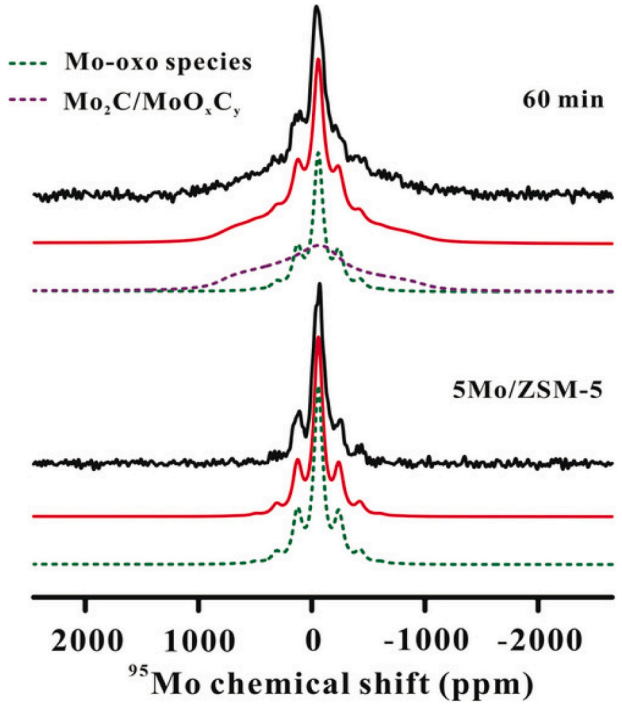

Fig. 10. Experimental and deconvoluted ^{95}Mo WURST-QCPMG MAS NMR spectra at 35.2 T of fresh 5Mo/ZSM-5 and 5Mo/ZSM-5 reacted for 60 min at 973 K. Reproduced from Ref. [169] with permission, Copyright 2021 Wiley-VCH.

quadrupolar products of ~6.9 MHz (ZIF-4 glass) and ~6.5–6.8 MHz (ZIF-62 glasses). This demonstrates that the ^{67}Zn NMR at ultra-high field serve as an excellent probe to detect the disorder around metal centers.

Due to very similar local environments, it is difficult to resolve different Zn sites in 1D ^{67}Zn MAS NMR spectra, even at ultra-high field of 35.2 T. The determination of inequivalent zinc sites in Sen *et al.*'s work still relies on the *priori* knowledge of crystal structure. In 2023, Huang *et al.* employed the MAS CryoProbe and a high field of 18.8 T to successfully acquire the ^{67}Zn 3QMAS spectra at natural abundance of two MOFs, ZIF-4 and $Zn_3(HCOO)_6$ within reasonable time, which enables the direct determination of inequivalent zinc sites in MOFs [203].

Zirconium-based MOFs are highly attractive materials owing to their exceptional chemical stability, tunable structures, and broad range of potential applications [204]. In Zr-MOFs, local disorder is commonly observed, and ^{91}Zr NMR is, in principle, a sensitive probe of the Zr coordination environment. However, ^{91}Zr NMR is experimentally challenging: ^{91}Zr (I = 5/2) possesses a very low gyromagnetic ratio (γ = 2.4975×10^7 rad T^{-1} s^{-1}), a modest natural abundance of 11.23%, and a moderate quadrupole moment (Q = 0.176 b) [159,202]. These nuclear properties lead to inherently broad and weak ^{91}Zr NMR signals. Advances in ultra-high magnetic field NMR have made it possible to directly investigate Zr centers in MOFs via ^{91}Zr solid-state NMR spectroscopy [187,188]. Huang *et al.* investigated the local structure around Zr using ^{91}Zr solid-state NMR up to 35.2 T [187]. A comparison of the ^{91}Zr NMR spectra of the textbook MOF UiO-66 and its analogue UiO-66-NH_2 is shown in Fig. 12. The topology and long-range order in the two MOFs are nearly the same, yielding very similar XRD patterns [187]. However, the ^{91}Zr solid-state NMR spectra are very different. In UiO-66-NH_2, the ^{91}Zr NMR spectrum is essentially featureless, reflecting a Gaussian-like distribution of local ^{91}Zr EFG parameters. This behavior contrasts sharply with the spectra of UiO-66, which displays well-resolved quadrupolar lineshapes indicative of a more ordered local structure.

Post-synthetic modification (PSM) has been proved as an effective approach to tailoring the MOF properties. For example, incorporating Ti metal centers into UiO-66(Zr) enables the tuning of the photocatalytic properties of UiO-66(Zr/Ti) [205,206]. Solid-state ^{47,49}Ti NMR is capable of probing subtle changes in the local environment induced by compositional variations. However, solid-state NMR of titanium remains intrinsically challenging due to the presence of two NMR-active quadrupolar isotopes, ^{47}Ti (I = 5/2, N.A. = 7.44%, Q = 302 mb) and ^{49}Ti (I = 7/2, N.A. = 5.41%, Q = 247 mb) [170,202]. These isotopes exhibit nearly identical gyromagnetic ratios (-1.5105×10^7 and -1.5110×10^7 rad T^{-1} s^{-1} for ^{47}Ti and ^{49}Ti, respectively) [170], leading to their simultaneous excitation under conventional experimental conditions. The combination of low natural abundance, moderate quadrupolar interactions, and closely spaced resonance frequencies substantially complicates both spectral acquisition and interpretation [207].

Moissette *et al.* employed ^{47,49}Ti NMR at a high field of 28.2 T to study the local structures of Ti in the mixed metallic MOF UiO-66(Zr/Ti) [208]. To exclude contributions from impurities, a reference $^{47/49}$Ti NMR spectrum of pure TiO_2 powder was recorded and compared with

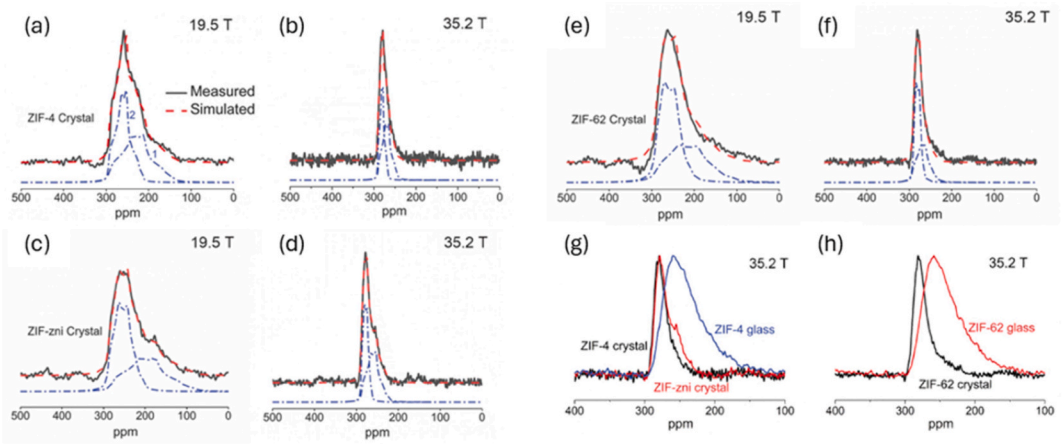

Fig. 11. (a-f) Experimental ^{67}Zn MAS NMR spectra (black) and corresponding simulations (red) for (a,b) ZIF-4, (c,d) ZIF-zni, and (e,f) ZIF-62 measured at 19.5 and 35.2 T. Individual simulation components (blue) are vertically offset for clarity. (g) Comparison of 35.2 T NMR spectra for ZIF-4 crystal, ZIF-zni crystal, and ZIF-4 glass. (h) Comparison of 35.2 T NMR spectra for ZIF-62 crystal and glass. Reproduced with permission from Ref. [13]. Copyright 2023 AAAS.

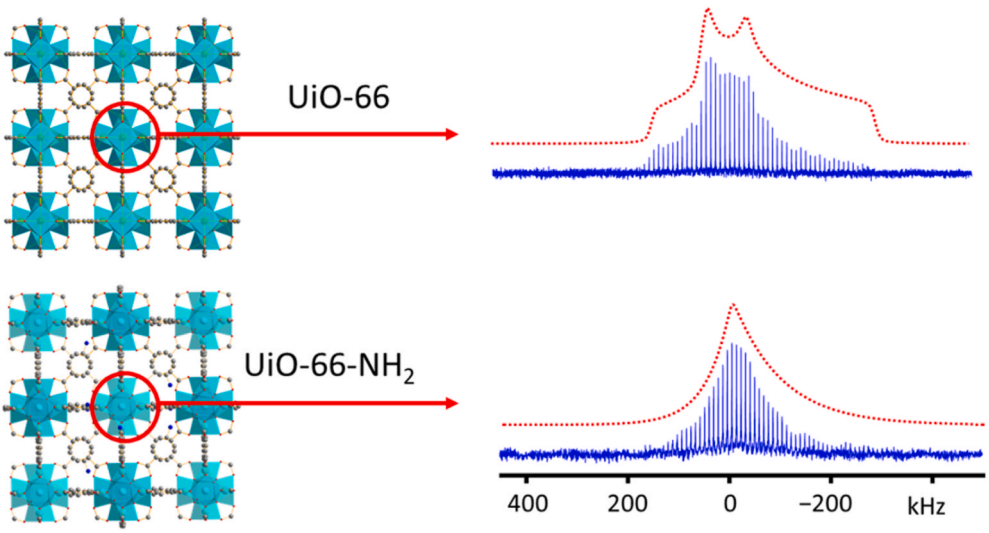

Fig. 12. Experimental (blue) and simulated (red) static ^{91}Zr QCPMG solid-state NMR spectra of UiO-66 and UiO-66-NH_2 obtained at a magnetic field of 35.2 T. Reproduced with permission from Ref. [187]. Copyright 2025 Royal Society of Chemistry.

the UiO-66(Zr/Ti) samples, confirming that the observed signals do not originate from precipitated TiO_2. Two samples of UiO-66(Zr/Ti) were studied: UiO-66(Zr/Ti)-OP (27 wt% Ti) is obtained from one-pot solvothermal reaction and the other is from post-synthetic modifications, denoted as UiO-66(Zr/Ti)-PSM (5 wt% Ti). The experimental and simulated $^{47/49}$Ti NMR spectra of both materials display broad, featureless line shapes without resolvable separation of the two isotopes (Fig. 13) [208]. Owing to this overlap and limited signal-to-noise ratio, only the ^{49}Ti contribution was considered for quantitative analysis. The distributed line shapes indicate a range of local environments rather than a single well-defined quadrupolar site; accordingly, a Czjzek model was employed to account for the distribution of electric field gradients. For ^{49}Ti, the reported C_Q in MIL-125(Ti), a titanium-based MOF constructed from BDC linkers is approximately 16 MHz [209], whereas UiO-66(Zr/Ti)-PSM and UiO-66(Zr/Ti)-OP exhibit values of 23.5 and 20 MHz, respectively. The increased C_Q values, together with the broadened and distributed line shapes, indicates a more distorted titanium coordination environment within UiO-66(Zr/Ti) compared to MIL-125 (Ti). Furthermore, the slightly lower C_Q observed for the PSM sample relative to the OP sample suggests that titanium incorporation via post-synthetic modification induces comparatively less local structural perturbation than direct incorporation during synthesis.

Apart from low-gyromagnetic ratio and low natural abundance, very large QI is another challenge for certain metal isotopes such as ^{209}Bi. ^{209}Bi ($I = 9/2$) has relatively large gyromagnetic ratio ($\gamma(^{209}\text{Bi}) = 4.375 \times 10^7$ rad T^{-1} s^{-1}), 100% natural abundance and exceptionally large quadrupole moments ($Q(^{209}\text{Bi}) = -516$ mb) [159,160,202]. ^{209}Bi solid-state NMR has been utilized to characterize functional inorganic complex oxides [195], half-heusler bismuthides [200], and organometallic compounds [210]. Recently, M. A. Hope *et al.* have investigated the perovskite using ^{209}Bi solid-state NMR at a high field of 28.2 T [77]. Huang *et al.* employed the ultra-high field up to 36 T and the field-stepping strategy to acquire the ^{209}Bi solid-state NMR spectra of representative MOFs [211]. Bismuth MOF IEF-3 ($Bi_2O_2(C_4O_4)$) are promising photocatalysts due to their semiconducting nature [212]. As shown in Fig. 14(a), IEF-3 contains a single Bi^{3+} site in a distorted square-pyramidal environment, yet its ^{209}Bi UW NMR spectrum, assembled from 100 field-stepped subspectra, covers *ca.* 45 MHz and exhibits multiple CT/ST features. Reliable simulation requires exact (non-perturbative) treatment because of the exceptionally large quadrupolar interaction ($\nu_Q/\nu_0 \approx 16\%$) and the field dependence of NMR parameters. The derived $C_Q = 860$ (2) MHz is among the largest reported

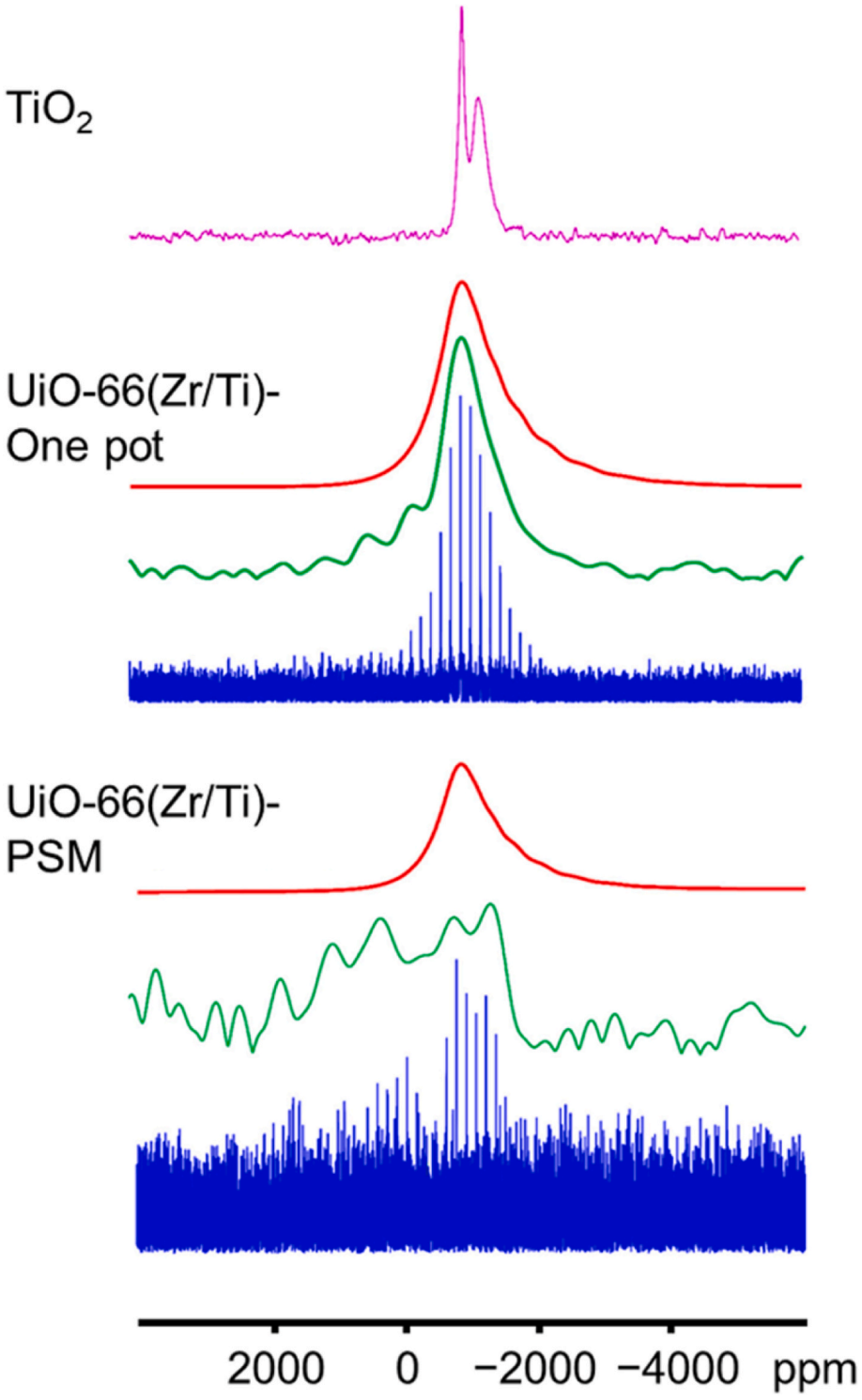

Fig. 13. Experimental 1D $^{47/49}$Ti QCPMG NMR spectra of UiO-66 (Zr/Ti)- PSM and UiO-66 (Zr/Ti)-One pot recorded under static conditions at 28.2 T. The envelope in green spectra results from the FT of the sum of the echoes. The red spectra correspond to the simulation. 1D $^{47/49}$Ti NMR quadrupolar echo spectrum of TiO_2 recorded under static conditions is shown on top. Figure reproduced from Ref. [208] with permission. Copyright 2026 American Chemical Society.

for ^{209}Bi and far exceeds values typical of non-MOF systems.

3.2.2. *Characterization of organic linkers*

Organic linkers in MOFs are composed of several NMR-active nuclei, including ^{1}H, ^{13}C, ^{14,15}N, ^{17}O, and ^{19}F. Solid-state NMR measurements on these linker atoms can reveal local structural environments that is often inaccessible by techniques such as XRD. The spin-1/2 nuclei such as ^{1}H, ^{13}C, ^{15}N (when enriched), and ^{19}F encompass high receptivity so they are usually accessible with low magnetic fields. However, the use of ^{17}O NMR for probing detailed structural and bonding information in linkers has long been hampered by its inherently low sensitivity and resolution, due to the isotope's extremely low natural abundance (0.038%), modest gyromagnetic ratio ($\gamma = -5.774$ MHz T^{-1}), and quadrupolar nature ($I = 5/2$) [159,202]. These challenges can be partially mitigated through isotope enrichment and ultra-high magnetic field. High field ^{17}O solid-state NMR spectroscopy has been employed to

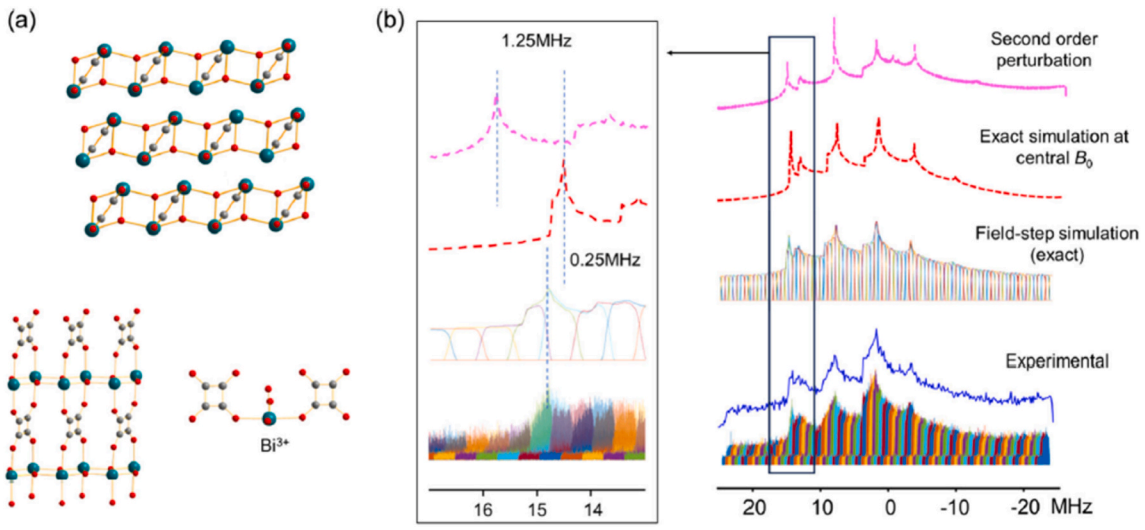

Fig. 14. (a) Layered structure of MOF IEF-3 and the Bi coordination geometry. (b) Experimental and simulated ^{209}Bi UW solid-state NMR spectra of IEF-3 using three simulation protocols. The magnified view of the "horn" at *ca.* 15 MHz is shown in the inset. Reproduced with permission from Ref. [211]. Copyright 2025 American Chemical Society.

characterize biological materials [36,37,51], and many organic compounds [52–54].

^{17}O NMR can serve as an alternative probe for detecting local environmental changes in mixed-metal MOFs. Ashbrook *et al.* studied the ion-exchanged Al,Ga-containing MOF MIL-53 (Fig. 15) [213]. Sample 1 is prepared by ion exchange of ^{17}O-enriched Al-MIL-53 as the parent material in $Ga_2(SO_4)_3$ solution. This enables ^{17}O NMR to directly monitor how Ga incorporation perturbs the local Al–O environments. Sample 2 is prepared by ion exchange of ^{17}O-enriched Ga-MIL-53 as the parent material in $Al_2(SO_4)_3$ solution. The ^{17}O MAS NMR at 23.5 T as shown in Fig. 15 were fitted using previously reported parameters for the three hydroxyl environments—Al–O(H)–Al, Al–O(H)–Ga, and Ga–O(H)–Ga. The relative signal intensities reveal Al:Ga ratios of 86:14 (sample 1) and 26:74 (sample 2). High-resolution ^{17}O MQMAS spectra

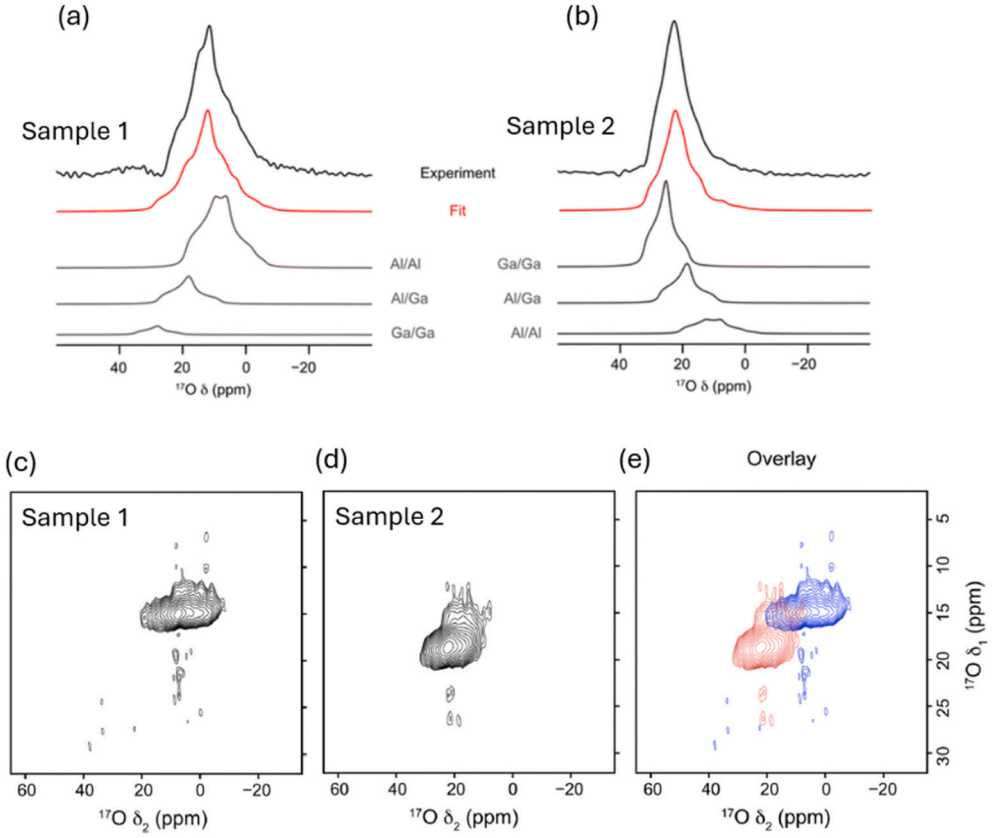

Fig. 15. ^{17}O 1D MAS NMR spectra (23.5 T, 20 kHz MAS) of (a) sample 1 and (b) sample 2. (c) and (d) show the corresponding ^{17}O MQMAS spectra of calcined (Al, Ga)-MIL-53 obtained after 5 days of framework/salt ion exchange, during which ^{17}O enrichment occurs. (e) Overlay of the MQMAS spectra in (c) and (d), with sample 1 shown in red and sample 2 in blue. Reproduced with permission from Ref. [213]. Copyright 2025 Royal Society of Chemistry.

can be collected within practical experimental times, typically requiring ~28–32 h depending on the number of t_1 increments. However, due to very similar oxygen isotropic shifts, the three signals weren't resolved even at 23.5 T. The same group also studied ^{17}O-enriched (Al,Sc)-MIL-53 materials with ^{17}O NMR at 23.5 T [214].

The thermal activation process of MOFs can also be tracked with high field ^{17}O NMR. Huang *et al.* studied the different oxygen species in MOF MIL-121, the structure of which is shown in Fig. 16(a) [215]. The ^{17}O 1D MAS NMR spectra of MIL-121-as (as-made) and MIL-121-ac (activated) at 19.6 and 35.2 T are shown in Fig. 16(b). At 19.6 T, four resonances appear at *ca.* 20, 175, 240, and 330 ppm, along with MAS spinning sidebands. Increasing the field to 35.2 T significantly sharpens the peaks, enhances the intensity of spinning sidebands due to the field-scaled chemical shift anisotropy, and reduces second-order QI. Based on chemical-shift ranges and structural information, the signals are assigned to O1 (μ_2-OH, 20 ppm), O5 (–COH, 175 ppm), O2/O3 (Al-bound CO_2^-, 240 ppm), and O4 (C=O of uncoordinated carboxylates, 330 ppm). Note that in MOF MIL-121-as, the oxygen sites on unreacted BTEC ligands (O21–O28) overlap with the framework signals and remain unresolved at 35.2 T due to their similar chemical environments

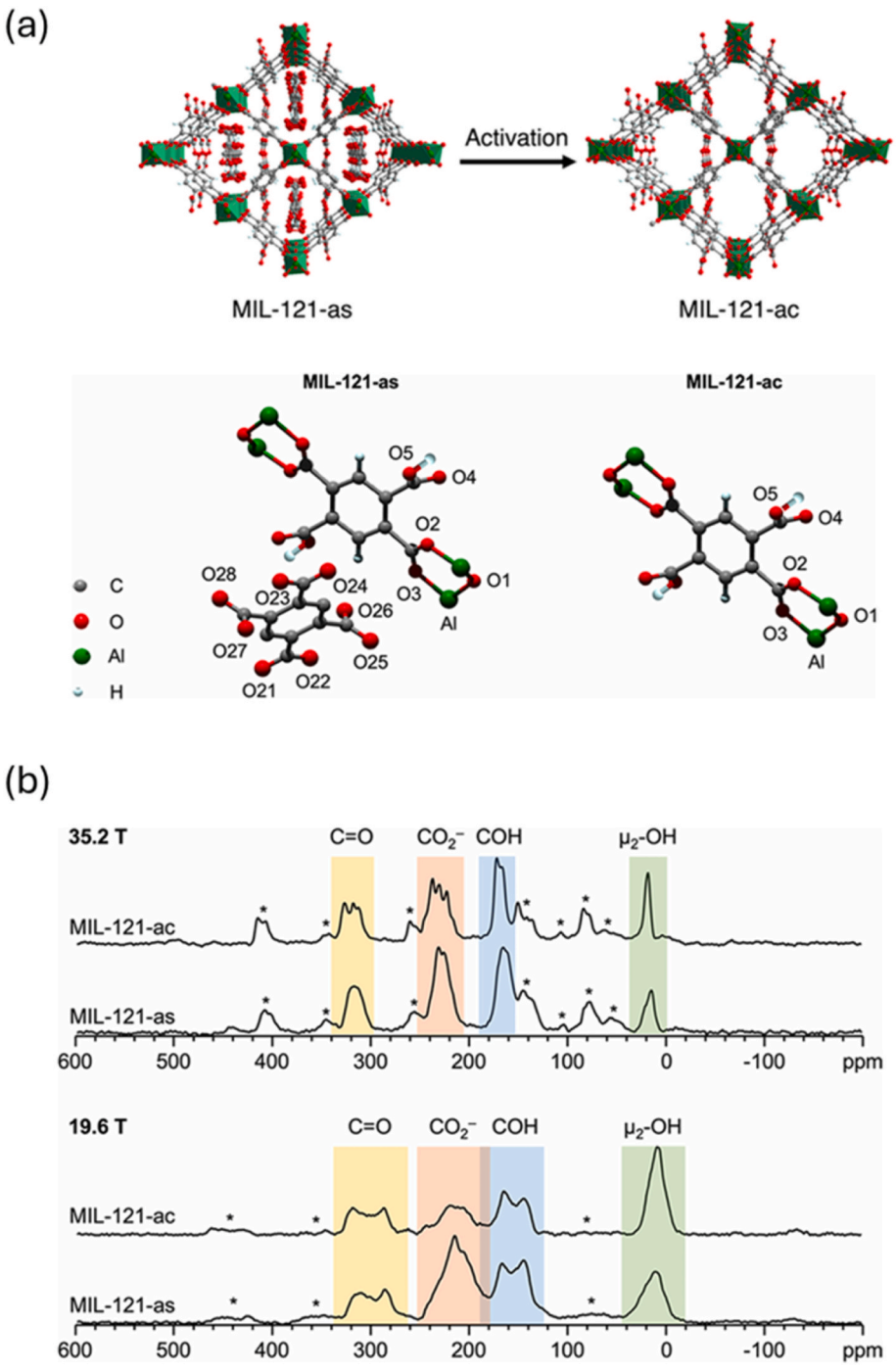

Fig. 16. (a) The schematic illustration of MIL-121-as and MIL-121-ac, along with five crystallographically distinct oxygen sites in MIL-121-as and MIL-121-ac labeled O1–O5. The additional eight unique oxygen sites on the uncoordinated BTEC ligands within the pores of MIL-121-as are labeled O21–O28. (b) ^{17}O 1D MAS NMR spectra of MIL-121-as and MIL-121-ac collected at 35.2 and 19.6 T with spinning rates of 18 and 16 kHz, respectively. Asterisks (*) mark the MAS spinning sidebands. Reproduced with permission from Ref. [215]. Copyright 2025 American Chemical Society.

and additional disorder-induced broadening. In addition, ^{17}O solid-state NMR was also used to distinguish the partially activated MOF MIL-53 from completely-activated MIL-53(Al) [216].

Besides MIL-121, Huang *et al.* studied the MOF α-$Mg_3(HCOO)_6$ which contains 12 crystallographically distinct oxygen sites [217]. To resolve these sites using ^{17}O NMR is extremely challenging as they have very similar local environments. The ^{17}O 2D 3QMAS spectra of the as-made and activated α-$Mg_3(HCOO)_6$ at 35.2 T (Fig. 17(a)) exhibit several well-resolved features along F_1, where 7 signals are distinguishable in the isotropic dimension for the as-made sample and 8 for the activated sample. This indicates that some F_1 features arise from multiple oxygen environments with nearly identical NMR parameters. With the aid of DFT calculations and 3QMAS, the corresponding simulated ^{17}O 1D MAS spectra (Fig. 17(b)) reproduce both the isotropic regions and the spinning sidebands reasonably well when quadrupolar and CSA contributions are included. The very high resolution allows one to detect subtle changes when there are guest molecules in the MOF [217]. In addition, the ^{17}O 3QMAS of MIL-53(Al), another textbook MOF, was also collected at 35.2 T (Fig. 17(c and d)) by the same group [216]. Four inequivalent oxygen sites were successfully resolved in the MIL-53(Al)-np form (Fig. 17(c and d)).

In addition to the organic linkers in MOFs, halide ions can also serve as important bridging components in MOFs [218]. The halide solid-state NMR has been applied in characterizing many materials [219,220], and there exists several excellent reviews on the halide NMR [221,222]. Iodide incorporation in MOFs can enhance catalytic performance, as demonstrated in Cu(I)–X–bpy MOFs (X = Cl, Br, I; bpy = 4,4′-bipyridine) that show activity for photocatalytic hydrogen production [223]. In the three-dimensional framework [CuI(bpy)], iodide bridges two Cu(I) centers in a μ_2 configuration (Fig. 18). Huang *et al.* reported its ^{127}I UW NMR spectrum at SCH using field-stepping approach [211]. The spectrum exhibits a quadrupolar-dominated powder pattern spanning ~20 MHz, reconstructed from 73 field-stepped subspectra acquired between 32.1 and 34.3 T. The powder pattern can be simulated with a single iodide site, consistent with the crystal structure. Upon thermal transformation to the two-dimensional phase [Cu_2I_2(bpy)], the iodide coordination changes from μ_2 to μ_3, leading to pronounced differences in the ^{127}I NMR spectra. The quadrupolar coupling constant increases from 290 (2) to 360 (2) MHz, while the asymmetry parameter η_Q decreases from 0.74 to 0.69, reflecting the altered local symmetry around the iodide site [211]. This case illustrates that ^{127}I UW solid-state NMR is a sensitive probe to detect structural changes induced by external stimuli.

3.2.3. *Characterization of guest-host interaction*

MOF guests can be probed via multi-nuclear NMR, *e.g.*, ^{13}C, ^{2}H, ^{17}O, ^{15}N [18,19,23]. CO_2 is a representative example of how solid-state NMR

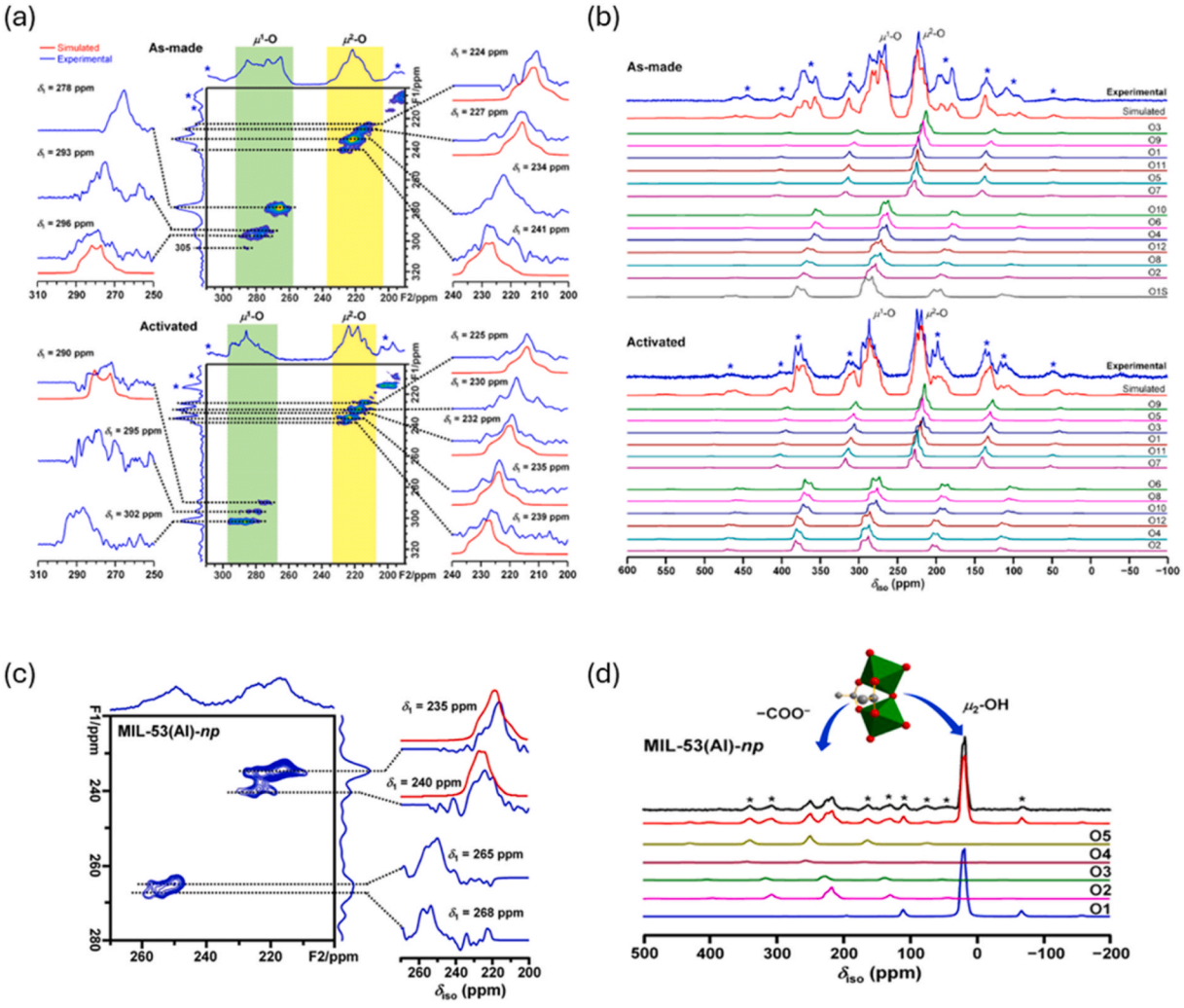

Fig. 17. (a) ^{17}O 2D 3QMAS NMR spectrum of ^{17}O-enriched α-$Mg_3(HCOO)_6$ recorded at 35.2 T, along with (b) experimental and simulated ^{17}O 1D MAS NMR spectra. (c) ^{17}O 2D 3QMAS spectra of ^{17}O-enriched MIL-53(Al)-np at 35.2 T. (d) Experimental and simulated ^{17}O 1D MAS NMR spectra of the MIL-53(Al)-np at 35.2 T. Asterisks (*) mark spinning sidebands (SSBs). (a,b) Reproduced with permission from Ref. [217]. Copyright 2025 American Chemical Society. (c,d) Reproduced with permission from Ref. [216], Copyright 2021 Wiley-VCH.

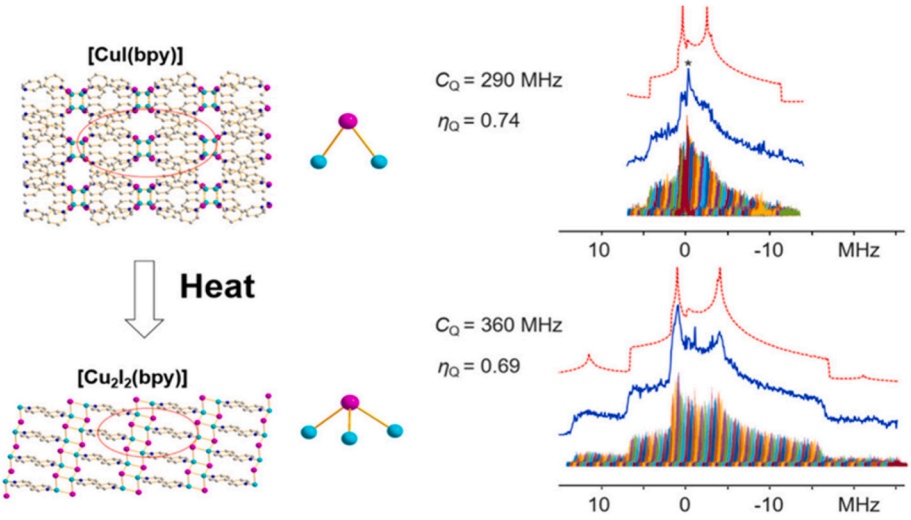

Fig. 18. Schematic representations of the MOF structures [CuI(bpy)] and [Cu_2I_2(bpy)], along with the corresponding experimental (blue) and simulated (red) ^{127}I UW solid-state NMR spectra. The sharp resonance marked by an asterisk near 0 ppm is due to a CuI impurity. Reproduced with permission from Ref. [211]. Copyright 2025 American Chemical Society.

can probe adsorption sites, locations, guest dynamics, and host–guest interactions in MOFs. ^{13}C solid-state NMR can be used to characterize the dynamics of $^{13}CO_2$ at low fields [224,225]. Another isotope which can be used is ^{17}O solid-state NMR at ultra-high fields.

Forse *et al.* studied the CO_2 adsorption mode in MOF (ii-2)-Mg_2 (dobpdc) with ^{17}O labeld CO_2 using ^{17}O solid-state NMR at 23.5 T [226]. As shown in Fig. 19, high-field ^{17}O NMR revealed that CO_2 adsorption in (ii-2)–Mg_2 (dobpdc) proceeds through an unexpected mixed ammonium carbamate–carbamic acid mechanism as illustrated by the clear carbamic acid resonance ($\delta_{iso} = 125.8$ ppm, $C_Q = 7.99$ MHz, $\eta_Q = 0.43$, Fig. 19 (a)), rather than forming pure carbamate chains as previously assumed. A distinct carbamic-acid ^{17}O resonance and complementary ^{13}C MAS and 2D ^{1}H–^{13}C correlation spectra (Fig. 19(c)) confirm the coexistence of two chemisorbed CO_2 environments in comparable proportions. DFT-supported structural analysis indicates alternating carbamate and carbamic-acid chains, suggesting that steric bulk from the ii-2 diamine

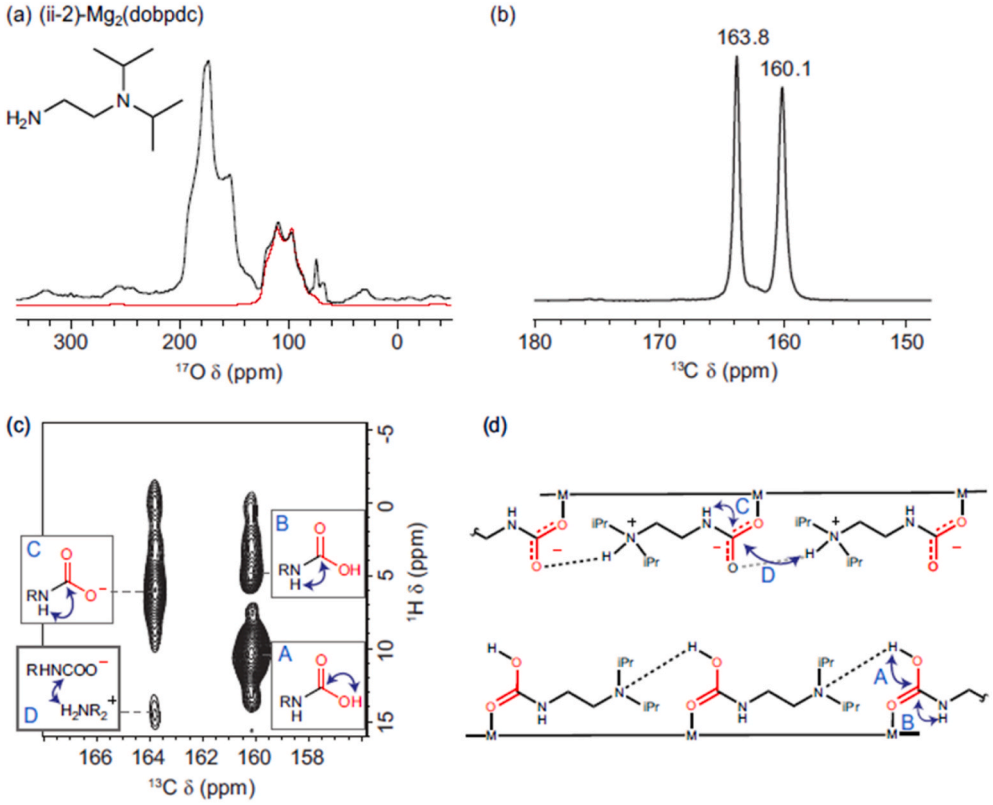

Fig. 19. (a) ^{17}O MAS NMR spectrum (23.5 T, 20 kHz MAS) of (ii-2)-Mg_2 (dobpdc) dosed with ^{17}O-enriched CO_2; the red trace corresponds to a carbamic-acid OH group. (b) ^{13}C MAS NMR spectrum (16.4 T, 15 kHz MAS) with cross polarization for (ii-2-Mg_2 (dobpdc)–CO_2 at 950 mbar $^{13}CO_2$. (c) ^{1}H→^{13}C HETCOR NMR spectrum (contact time 100 μs). (d) DFT-optimized Lewis structure illustrating the corresponding functional groups. Reproduced with permission from Ref. [226]. Copyright 2022 Springer.

promotes carbamic-acid formation [226].

Forse *et al.* also applied ^{17}O NMR to the benchmark hydroxide-based CO_2 sorbent MFU-4l ($Zn_5(OH)_4$ (btdd)$_3$) [227], which contains well-defined monodentate Zn–OH sites expected to form bicarbonate species upon CO_2 insertion. As shown in Fig. 20(B), the ^{17}O MAS NMR spectrum of $C^{17}O_2$-dosed MFU-4l shows four clear signals assignable to physisorbed CO_2, carbonyl and hydroxyl groups of bicarbonate, and residual Zn–OH. The observed 2:1 ratio of carbonyl to hydroxyl resonances is consistent with the established bicarbonate binding mode. Notably, reduced quadrupolar broadening and the collapse of the two inequivalent carbonyl environments predicted by DFT are indicative of dynamic motion at the Zn–OH site that partially averages the quadrupolar interaction. These dynamics at weakly binding sites were further supported by investigation using molecular dynamics simulations [227].

Recently, they collected the 1D PRESTO (phase shifted recoupling effects a smooth transfer of order) spectra, which is employed as a spectral-editing approach to selectively enhance the bicarbonate hydroxyl signal at $\delta_{obs} \approx 100$ ppm, thereby directly identifying the oxygen site bonded to a proton and confirming its assignment [228]. Further ^{17}O–^{1}H D-RINEPT NMR experiments enables detection of both short- and longer-range dipolar correlations. Additional cross-peaks reveal interactions between the bicarbonate carbonyl oxygen (δ_{obs} (^{17}O) $\approx$ 180 ppm) and adjacent aromatic framework protons ($\delta(^{1}H) = 7.7$ ppm), as well as correlations involving unreacted or defect Zn–OH sites (δ_{obs} (^{17}O) ≈ -60 ppm) with both framework and hydroxide protons. Notably, these Zn–OH resonances become observable due to reversible CO_2 binding that facilitates ^{17}O isotopic exchange. These results highlight the power of ^{17}O–^{1}H solid-state NMR methodologies for probing CO_2 capture chemistry. In contrast to conventional ^{13}C–^{1}H NMR or IR spectroscopy, the use of enriched $C^{17}O_2$ selectively restricts spectral observation to the dosed CO_2 and chemically involved oxygen environments, effectively suppressing background signals from the organic framework. The complementary nature of PRESTO and D-RINEPT further enhances structural resolution: PRESTO, subject to dipolar truncation, selectively emphasizes the strongest short-range dipolar interactions and is therefore particularly effective for spectral editing, whereas D-RINEPT, unaffected by dipolar truncation, enables more comprehensive mapping of both short- and long-range correlations.

Besides the adsorption of CO_2, Wang *et al.* used the $^{1}H\{^{14}N\}$ D-HMQC at high field of 23.5 T to characterize the NO_2 adsorption site in MOF MFM-305-CH3 [229]. As shown in Fig. 21, upon NO_2 adsorption, the ^{14}N chemical shift of the methylpyridinium site in the organic linker 1-methylpyridiniumdicarboxylate shows a small change and an additional upfield resonance appears in the 2D ^{14}N–^{1}H correlation spectrum. Neither signal aligns with the expected ^{14}N frequency of confined NO_3^-, suggesting that the adsorbed species undergoes rapid motion that averages the ^{14}N–^{1}H dipolar coupling. The two ^{14}N resonances in NO_2@MFM-305-CH_3 further indicate NO_2-induced structural perturbations at the methylpyridinium N centre. The new correlations between these ^{14}N signals and the 4.6-ppm methyl protons reveal a slowdown of methyl rotation, likely due to hydrogen bonding, which enhances dipolar-mediated $^{1}H \rightarrow {}^{14}N$ polarization transfer.

4. Conclusion and outlook

Ultra-high magnetic fields at 1 GHz and beyond have substantially advanced solid-state NMR studies of microporous materials. As discussed in this review, the gains in sensitivity and spectral resolution provided by GHz-class magnets have broadened the range of nuclei and structural features that can be reliably investigated in zeolites and MOFs. Nuclei that were previously difficult to observe due to low gyromagnetic ratios, low natural abundance, or strong quadrupolar interactions have become increasingly accessible. In particular, the reduction of second-order quadrupolar broadening, together with improved chemical shift dispersion and signal-to-noise ratios, has enabled more broad characterization of framework heteroatoms, metal

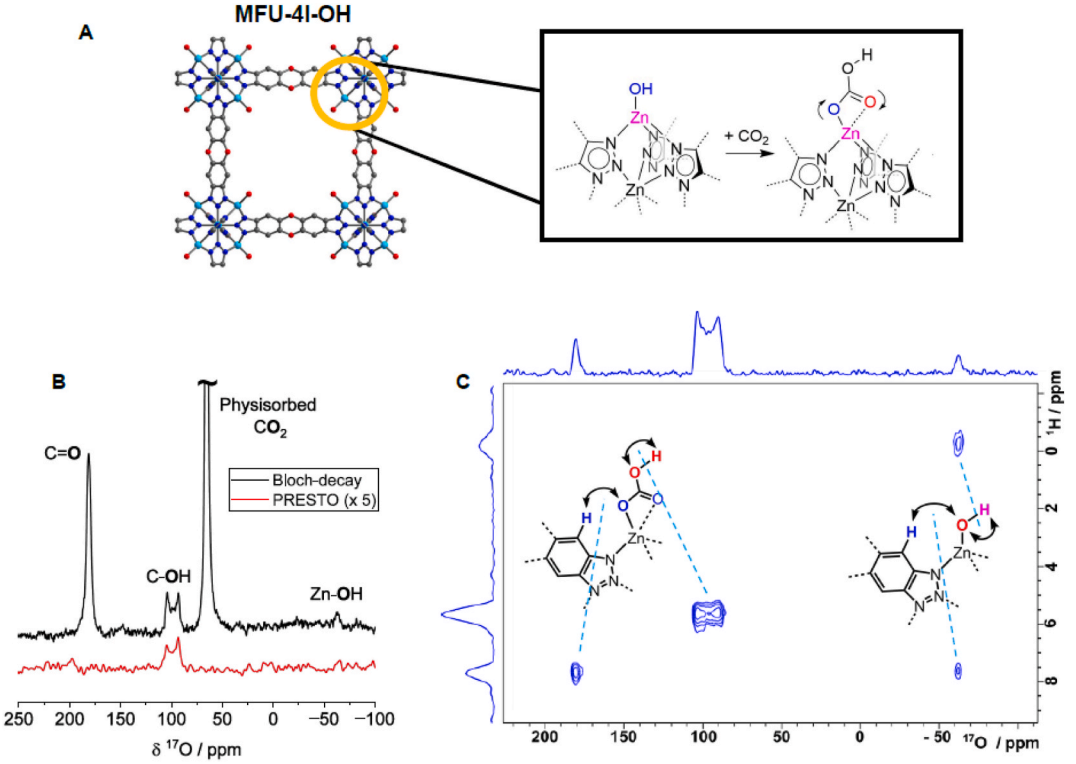

Fig. 20. (A) Crystal structure of cubic MFU-4l, with an inset illustrating the proposed CO_2 capture mechanism. (B) Comparison between a single-pulse NMR spectrum (23.5 T, 20 kHz MAS) and a^{17}O–^{1}H PRESTO 1D experiment (23.5 T, 12.5 kHz MAS) using a 175 μs recoupling time. (C) Two-dimensional ^{17}O–^{1}H D-RINEPT spectrum at 22.3 T (20 kHz MAS) with a 400 μs recoupling time. Figure reproduced from Ref. [228] with permission.

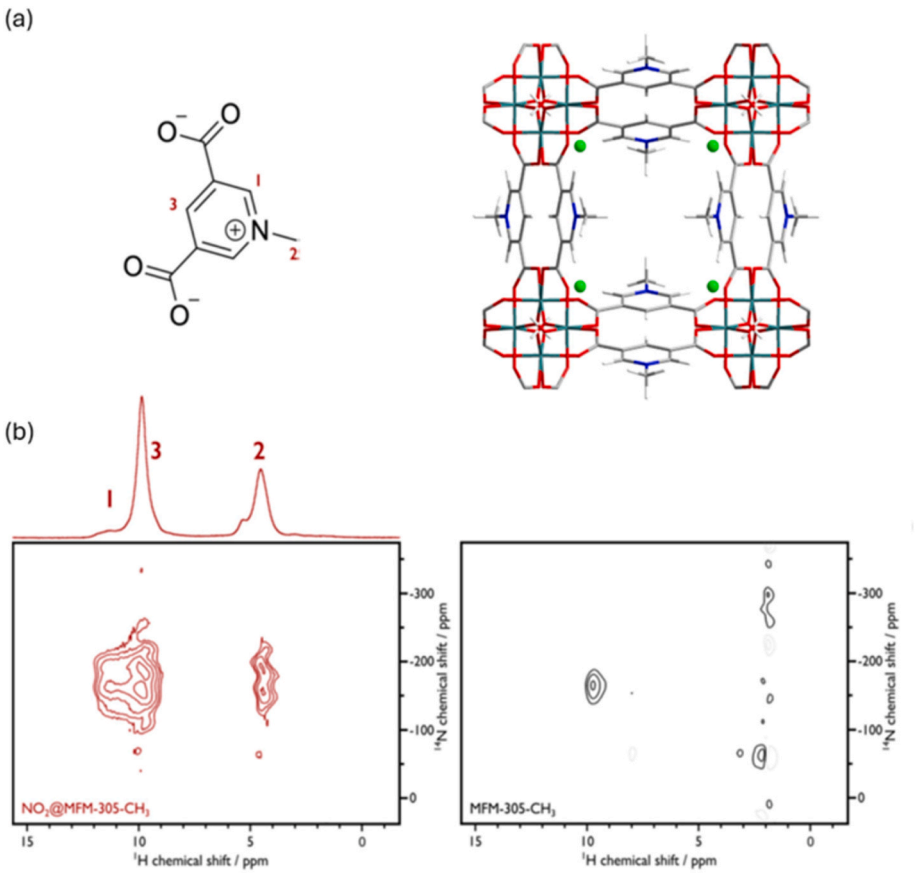

Fig. 21. (a) The organic linker 1-methylpyridiniumdicarboxylate and schematic illustration of MOF MFM-305-CH_3. (b) 2D ^{14}N-^{1}H D-HMQC NMR spectra of NO_2@MFM-305-CH_3 and MFM-305-CH_3. Reproduced from Ref. [229]. Copyright 2025 Wiley-VCH.

centers, organic linkers, and host–guest interactions.

Future progress in high-field NMR will be closely linked to ongoing advances in instrumentation and methodological innovation. Cryogenic MAS probe technology offers further sensitivity improvements, which are especially valuable for dilute or low-γ nuclei. The combination of ultra-high magnetic fields with dynamic nuclear polarization (DNP) provides additional opportunities to investigate surfaces, interfaces, and low-concentration active sites. Advances in pulse sequence design, including methods tailored for quadrupolar nuclei, multidimensional correlation experiments, and fast magic-angle spinning, will further enhance the structural information obtainable from complex and disordered systems. At the same time, the integration of experimental NMR with density functional theory (DFT) calculations and emerging artificial intelligence (AI)-driven approaches will continue to improve spectral interpretation and structural assignment. The enhanced performance at GHz fields also facilitates in situ and operando investigations under conditions relevant to adsorption, catalysis, and framework transformation. Such studies are important for establishing structure–property relationships and for gaining mechanistic insight at the atomic level.

Overall, ultra-high field solid-state NMR at 1 GHz and beyond represents a significant step forward in the characterization of microporous materials. Continued technical and methodological refinement, together with closer integration of experiment and theory, will further strengthen its role in advancing fundamental understanding and materials development.

Declaration of competing interest

The authors declare that they have no known competing financial interests or personal relationships that could have appeared to influence the work reported in this paper.

Acknowledgement

Y.H. thanks the Natural Science and Engineering Research Council (NSERC) of Canada for a Discovery Grant. The National High Magnetic Field Laboratory is supported by the National Science Foundation through NSF/DMR-1644779, NSF/DMR-2128556 and the State of Florida. The 36 T Series Connected Hybrid (SCH) magnet was supported by NSF (DMR-1039938 and DMR0603042) with NMR instrumentation developed by the NIH National Resource for Advanced NMR Technology (NIH RM1 GM14867 and NIH BTRR 1P41 GM122698). The graphical abstract incorporates elements adapted from an image by the Database Centre for Life Science (DBCLS), licensed under CC BY 3.0.

Data availability

No data was used for the research described in the article.

References

[1] K. Chen, S.H. Mousavi, R. Singh, R.Q. Snurr, G. Li, P.A. Webley, Gating effect for gas adsorption in microporous materials—mechanisms and applications, Chem. Soc. Rev. 51 (2022) 1139–1166.
[2] R.E. Morris, P.S. Wheatley, Gas storage in nanoporous materials, Angew. Chem. Int. Ed. 47 (2008) 4966–4981.
[3] F. Chang, J. Zhou, P. Chen, Y. Chen, H. Jia, S.M. Saad, Y. Gao, X. Cao, T. Zheng, Microporous and mesoporous materials for gas storage and separation: a review, Asia Pac. J. Chem. Eng. 8 (2013) 618–626.
[4] B. Li, H. Wang, B. Chen, Microporous metal–organic frameworks for gas separation, Chem. Asian J. 9 (2014) 1474–1498.
[5] X. Zou, G. Zhu, Microporous organic materials for membrane-based gas separation, Adv. Mater. 30 (2018) 1700750.

[6] R.-B. Lin, S. Xiang, W. Zhou, B. Chen, Microporous metal-organic framework materials for gas separation, Chem 6 (2020) 337–363.
[7] A. Corma, From microporous to mesoporous molecular sieve materials and their use in catalysis, Chem. Rev. 97 (1997) 2373–2420.
[8] J. Weitkamp, M. Hunger, U. Rymsa, Base catalysis on microporous and mesoporous materials: recent progress and perspectives, Microporous Mesoporous Mater. 48 (2001) 255–270.
[9] N. Huang, P. Wang, D. Jiang, Covalent organic frameworks: a materials platform for structural and functional designs, Nat. Rev. Mater. 1 (2016) 1–19.
[10] B.M. Weckhuysen, J. Yu, Recent advances in zeolite chemistry and catalysis, Chem. Soc. Rev. 44 (2015) 7022–7024.
[11] J. Lee, J. Kim, T. Hyeon, Recent progress in the synthesis of porous carbon materials, Adv. Mater. 18 (2006) 2073–2094.
[12] H. Furukawa, K.E. Cordova, M. O'Keeffe, O.M. Yaghi, The chemistry and applications of metal-organic frameworks, Science 341 (2013) 1230444.
[13] R.S. Madsen, A. Qiao, J. Sen, I. Hung, K. Chen, Z. Gan, S. Sen, Y. Yue, Ultrahigh-field ^{67}Zn NMR reveals short-range disorder in zeolitic imidazolate framework glasses, Science 367 (2020) 1473–1476.
[14] B. Reif, S.E. Ashbrook, L. Emsley, M. Hong, Solid-state NMR spectroscopy, Nat. Rev. Methods Primers 1 (2021) 2.
[15] S.P. Brown, H.W. Spiess, Advanced solid-state NMR methods for the elucidation of structure and dynamics of molecular, macromolecular, and supramolecular systems, Chem. Rev. 101 (2001) 4125–4156.
[16] S.E. Ashbrook, D.M. Dawson, V.R. Seymour, Recent developments in solid-state NMR spectroscopy of crystalline microporous materials, Phys. Chem. Chem. Phys. 16 (2014) 8223–8242.
[17] H.C. Hoffmann, M. Debowski, P. Müller, S. Paasch, I. Senkovska, S. Kaskel, E. Brunner, Solid-state NMR spectroscopy of metal–organic framework compounds (MOFs), Materials 5 (2012) 2537–2572.
[18] B.E. Lucier, S. Chen, Y. Huang, Characterization of metal–organic frameworks: unlocking the potential of solid-state NMR, Acc. Chem. Res. 51 (2018) 319–330.
[19] Y.A. Wong, V. Martins, B.E. Lucier, Y. Huang, Solid-state NMR spectroscopy: a powerful technique to directly study small gas molecules adsorbed in metal–organic frameworks, Chem. Eur J. 25 (2019) 1848–1853.
[20] A. Sutrisno, Y. Huang, Solid-state NMR: a powerful tool for characterization of metal–organic frameworks, Solid State Nucl. Magn. Reson. 49 (2013) 1–11.
[21] G. Qi, Q. Wang, J. Xu, F. Deng, Solid-state NMR studies of internuclear correlations for characterizing catalytic materials, Chem. Soc. Rev. 50 (2021) 8382–8399.
[22] E. Brunner, M. Rauche, Solid-state NMR spectroscopy: an advancing tool to analyse the structure and properties of metal–organic frameworks, Chem. Sci. 11 (2020) 4297–4304.
[23] V.J. Witherspoon, J. Xu, J.A. Reimer, Solid-state NMR investigations of carbon dioxide gas in metal–organic frameworks: insights into molecular motion and adsorptive behavior, Chem. Rev. 118 (2018) 10033–10048.
[24] S. Li, O. Lafon, W. Wang, Q. Wang, X. Wang, Y. Li, J. Xu, F. Deng, Recent advances of solid-state NMR spectroscopy for microporous materials, Adv. Mater. 32 (2020) 2002879.
[25] G. Paul, C. Bisio, I. Braschi, M. Cossi, G. Gatti, E. Gianotti, L. Marchese, Combined solid-state NMR, FT-IR and computational studies on layered and porous materials, Chem. Soc. Rev. 47 (2018) 5684–5739.
[26] J. Xu, Q. Wang, F. Deng, Metal active sites and their catalytic functions in zeolites: insights from solid-state NMR spectroscopy, Acc. Chem. Res. 52 (2019) 2179–2189.
[27] S. Li, F. Deng, Recent advances of solid-state NMR studies on zeolites, Annu. Rep. NMR Spectrosc. 78 (2013) 1–54.
[28] H. Lechert, G. Engelhardt, D. Michel, High Resolution Solid State NMR of Silicates and Zeolites, John Wiley & Sons, Chichester, New York, Brisbane, Toronto, Singapore, 1988.
[29] J. Xu, Q. Wang, S. Li, F. Deng, Solid-State NMR in Zeolite Catalysis, Springer, 2019.
[30] W. Wang, S. Chen, Y. Huang, NMR of Metal–Organic Frameworks and Covalent Organic Frameworks, Royal Society of Chemistry, 2024.
[31] P. Wikus, W. Frantz, R. Kümmerle, P. Vonlanthen, Commercial gigahertz-class NMR magnets, Supercond. Sci. Technol. 35 (2022) 033001.
[32] Ultra-High Field NMR Whitepaper, (n.d.). https://www.bruker.com/en/products-and-solutions/mr/nmr/ascend-ghz-class.html.
[33] Z. Gan, I. Hung, X. Wang, J. Paulino, G. Wu, I.M. Litvak, P.L. Gor'kov, W.W. Brey, P. Lendi, J.L. Schiano, NMR spectroscopy up to 35.2 T using a series-connected hybrid magnet, J. Magn. Reson. 284 (2017) 125–136.
[34] C.M. Quinn, M. Wang, T. Polenova, NMR of macromolecular assemblies and machines at 1 GHz and beyond: new transformative opportunities for molecular structural biology, Protein NMR Methods Protoc. (2017) 1–35.
[35] S.G. Patching, Ultra-high field Nuclear Magnetic Resonance (NMR) spectroscopy: applications at 1 GHz and beyond. https://doi.org/10.31219/osf.io/gte42, 2024.
[36] J. Špačková, C. Fabra, S. Mittelette, E. Gaillard, C.-H. Chen, G. Cazals, A. Lebrun, S. Sene, D. Berthomieu, K. Chen, Z. Gan, C. Gervais, T.-X. Métro, D. Laurencin, Unveiling the structure and reactivity of fatty-acid based (Nano)materials thanks to efficient and scalable ^{17}O and^{18}O-Isotopic Labeling Slhemes, Js Am. Chem. Soc. 142 (2020) 21068–21081.
[37] R. Zhang, T.A. Cross, X. Peng, R. Fu, Surprising rigidity of functionally important water molecules buried in the lipid headgroup region, J. Am. Chem. Soc. 144 (2022) 7881–7888.
[38] M. Callon, A.A. Malär, S. Pfister, V. Římal, M.E. Weber, T. Wiegand, J. Zehnder, M. Chávez, R. Cadalbert, R. Deb, Biomolecular solid-state NMR spectroscopy at 1200 MHz: the gain in resolution, J. Biomol. NMR 75 (2021) 255–272.
[39] S. Zager, N. Medved, M. Cevec, U. Čerček, B. Rogelj, J. Plavec, J. Kragelj, Fast MAS NMR spectroscopy can identify G-Quartets and double-stranded structures in aggregates formed by GGGGCC RNA repeats, bioRxiv (2025), 2025–09.
[40] R. Pylkkänen, D. Werner, A. Bishoyi, D. Weil, E. Scoppola, W. Wagermaier, A. Safeer, S. Bahri, M. Baldus, A. Paananen, The complex structure of Fomes fomentarius represents an architectural design for high-performance ultralightweight materials, Sci. Adv. 9 (2023) eade5417.
[41] S. Wang, T. Ravula, J.A. Stringer, P.L. Gor'kov, O.A. Warmuth, C.G. Williams, A. F. Thome, L.J. Mueller, C.M. Rienstra, Ultrahigh-resolution solid-state NMR for high–molecular weight proteins on GHz-class spectrometers, Sci. Adv. 11 (2025) eadx6016.
[42] O. Saurel, I. Iordanov, G. Nars, P. Demange, T. Le Marchand, L.B. Andreas, G. Pintacuda, A. Milon, Local and global dynamics in Klebsiella pneumoniae outer membrane protein a in lipid bilayers probed at atomic resolution, J. Am. Chem. Soc. 139 (2017) 1590–1597.
[43] M. Callon, D. Luder, A.A. Malär, T. Wiegand, V. Římal, L. Lecoq, A. Böckmann, A. Samoson, B.H. Meier, High and fast: NMR protein–proton side-chain assignments at 160 kHz and 1.2 GHz, Chem. Sci. 14 (2023) 10824–10834.
[44] T. Schubeis, T.S. Schwarzer, T. Le Marchand, J. Stanek, K.T. Movellan, K. Castiglione, G. Pintacuda, L.B. Andreas, Resonance assignment of the outer membrane protein AlkL in lipid bilayers by proton-detected solid-state NMR, Biomol. NMR Assign. 14 (2020) 295–300.
[45] E. Nimerovsky, K.T. Movellan, X.C. Zhang, M.C. Forster, E. Najbauer, K. Xue, R. Dervişoğlu, K. Giller, C. Griesinger, S. Becker, Proton detected solid-state NMR of membrane proteins at 28 Tesla (1.2 GHz) and 100 kHz magic-angle spinning, Biomolecules 11 (2021) 752.
[46] K. Xue, R. Sarkar, Z. Tosner, D. Lalli, C. Motz, B. Koch, G. Pintacuda, B. Reif, MAS dependent sensitivity of different isotopomers in selectively methyl protonated protein samples in solid state NMR, J. Biomol. NMR 73 (2019) 625–631.
[47] M. Dinclaux, E. Cahoreau, P. Millard, F. Létisse, G. Lippens, Increasing field strength versus advanced isotope labeling for NMR-based fluxomics, Magn. Reson. Chem. 58 (2020) 305–311.
[48] L. Dsouza, X. Li, V. Erić, A. Huijser, T.L. Jansen, A.R. Holzwarth, F. Buda, D. A. Bryant, S. Bahri, K.B.S.S. Gupta, An integrated approach towards extracting structural characteristics of chlorosomes from a bchQ mutant of Chlorobaculum tepidum, Phys. Chem. Chem. Phys. 26 (2024) 15856–15867.
[49] S. Bahri, A. Safeer, A. Adler, H. Smedes, H. van Ingen, M. Baldus, ^{1}H-detected characterization of carbon–carbon networks in highly flexible protonated biomolecules using MAS NMR, J. Biomol. NMR 77 (2023) 111–119.
[50] E. Barbet-Massin, A.J. Pell, J.S. Retel, L.B. Andreas, K. Jaudzems, W.T. Franks, A. J. Nieuwkoop, M. Hiller, V. Higman, P. Guerry, Rapid proton-detected NMR assignment for proteins with fast magic angle spinning, J. Am. Chem. Soc. 136 (2014) 12489–12497.
[51] I. Hung, E.G. Keeler, W. Mao, P.L. Gor'kov, R.G. Griffin, Z. Gan, Residue-specific high-resolution ^{17}O Solid-Statsolid-sar Mannetic Rmsonance rf Peptides: pultidimenmional Indirect ^{1}i Detection and Mdgic-Angle Spimagic-a, J. Phss. Chem. Lett. 13 (2022) 6549–6558.
[52] B. Lin, I. Hung, Z. Gan, P. Chien, H.L. Spencer, S.P. Smith, G. Wu, ^{17}O NMR studies of yeast ubiquitin in aqueous solution and in the solid state, Chembiochem 22 (2021) 826–829.
[53] J. Shen, V. Terskikh, J. Struppe, A. Hassan, M. Monette, I. Hung, Z. Gan, A. Brinkmann, G. Wu, Solid-state ^{17}O NMR study of α-d-glucose: exploring new frontiers in isotopic labeling, sensitivity enhancement, and NMR crystallography, Chem. Sci. 13 (2022) 2591–2603.
[54] J. Shen, V. Terskikh, X. Wang, I. Hung, Z. Gan, G. Wu, A quadrupole-central-transition ^{17}O NMR Study of Nicotinamine: Experimentel Evidence oe Cross-Corrcross-c between Second-Ordsecond-oupolaq Interactioi and Magnetic Smielding snisotropy, J. Phys. Chem. B 122 (2018) 4813–4820.
[55] A.J. Stirk, S.T. Holmes, F.E.S. Souza, I. Hung, Z. Gan, J.F. Britten, A.W. Rey, R. W. Schurko, An unusual ionic cocrystal of ponatinib hydrochloride: characterization by single-crystal X-ray diffraction and ultra-high field NMR spectroscopy, CrystEngComm 26 (2024) 1219–1233.
[56] N. Schröder, E. Bartalucci, T. Wiegand, Probing noncovalent interactions by fast magic-angle spinning NMR at 100 kHz and more, ChemPhysChem 25 (2024) e202400537.
[57] A.A. Malär, Q. Sun, J. Zehnder, G. Kehr, G. Erker, T. Wiegand, Proton-phosphorous connectivities revealed by high-resolution proton-detected solid-state NMR, Phys. Chem. Chem. Phys. 24 (2022) 7768–7778.
[58] N. Thomas, S. Moussaoui, B. Reyes-Suárez, O. Lafon, G.N.M. Reddy, Dual cross-linked cellulose based hydrogel films, Mater. Adv. 5 (2024) 9210–9219.
[59] P.M.J. Szell, Z. Rehman, B.P. Tatman, L.P. Hughes, H. Blade, S.P. Brown, Exploring the potential of multinuclear solid-state ^{1}H,^{13}C, and ^{35}Cl Magnetic Resonamce To ChrracterizetSctic and Dynasic Disorded in Phadmaceutical pydrochlorides, ChemPhysChem 24 (2023) e202200558.
[60] Y. Xu, M. Calabrese, N. Demitri, A. Pizzi, T. Nag, I. Hung, Z. Gan, G. Resnati, D. L. Bryce, Non-covalent matere bonds in perrhenates probed *via* ultrahigh field rhenium-185/187 NMR and zero-field NQR spectroscopy, Chem. Commun. 59 (2023) 12609–12612.
[61] S.T. Holmes, J. Schönzart, A.B. Philips, J.J. Kimball, S. Termos, A.R. Altenhof, Y. Xu, C.A. O'Keefe, J. Autschbach, R.W. Schurko, Structure and bonding in rhodium coordination compounds: a ^{103}Rh solid-state NMR and relativistic DFT study, Chem. Sci. 15 (2024) 2181–2196.
[62] S.T. Holmes, Y. Xu, A.B. Philips, S. Termos, J.J. Kimball, J. Autschbach, R. W. Schurko, ^{99}Ru solid-state nuclear magnetic resonance spectroscopy of organometallic compounds: linking nuclear magnetic resonance parameters with metal–ligand bonding, J. Am. Chem. Soc. 147 (2025) 20865–20877.

[63] B.A. Atterberry, P. Paluch, A.R. Lamkins, W. Huang, A.J. Rossini, Rapid acquisition of ^{103}Rh Solid-State NMRsolid-sa by ^{31}P setection and Sideband Sedective Methods, J. Am.sChem. Socm 147 (2025) 14411–14421.

[64] E. Bartalucci, A.A. Malär, A. Mehnert, J.B. Kleine Büning, L. Günzel, M. Icker, M. Börner, C. Wiebeler, B.H. Meier, S. Grimme, B. Kersting, T. Wiegand, Probing a Hydrogen-π interaction involving a trapped water molecule in the solid state, Angew. Chem. Int. Ed. 62 (2023) e202217725.

[65] K. Szeto, M. Taoufik, F. Fayon, D. Gajan, E. Zurek, J. Autschbach, J. Trébosc, L. Delevoye, R.M. Gauvin, Evidence for methylaluminoxane (MAO) molecular structure and reactivity from ultrahigh magnetic field ^{27}Al MAS NMR Spectroscosy Combined wcth DFT Calculatiocs, Angew. Chem. Int. Ed. 64 (2025) e202508409.

[66] I. Goldberga, I. Hung, V. Sarou-Kanian, C. Gervais, Z. Gan, J. Novák-Špačková, T.-X. Métro, C. Leroy, D. Berthomieu, A. Van Der Lee, C. Bonhomme, D. Laurencin, High-resolution ^{17}O Solid-Statsolid-ss a Unique Proue for pnvestigating Oxalate Bioding Mobes in Mmterials:mThe Case Studycof Calcium Oxclate Biomineralb, Inorg. Chem. 63 (2024) 10179–10193.

[67] I. Goldberga, N.D. Jensen, C. Combes, F. Mentink-Vigier, X. Wang, I. Hung, Z. Gan, J. Trébosc, T.-X. Métro, C. Bonhomme, C. Gervais, D. Laurencin, ^{17}O solid state NMR as a valuable tool for deciphering reaction mechanisms in mechanochemistry: the case study on the ^{17}O-enrichment of hydrated Ca-pyrophosphate biominerals, Faraday Discuss 241 (2023) 250–265.

[68] E. Bellan, F. Maleki, M. Jakoobi, P. Fau, K. Fajerwerg, D. Lagarde, A. Balocchi, P. Lecante, J. Trébosc, Y. Xu, Z. Gan, L. Pautrot-d'Alençon, T. Le Mercier, H. Nagashima, G. Pacchioni, O. Lafon, Y. Coppel, M.L. Kahn, Ultra-high-field ^{67}Zn and ^{33}S NMR Studies Coupled withsDFT Calculations Reveal che Structurerof ZnS Nansplatelets Preparnd by an Organpmetallic Approoch, J. Phys. Caem. C 127 (2023) 17809–17819.

[69] H.J. Jakobsen, H. Bildsøe, M. Bondesgaard, B.B. Iversen, M. Brorson, F.H. Larsen, Z. Gan, I. Hung, Exciting opportunities for solid-state ^{95}Mo NMR Studies ofsMoS_2 Nanostructnres in Materials mesearch from a Low to an lltrahigh uagnetic Fmeld (35.f T), J. Phys. Chem. C 125 (2021) 7824–7838.

[70] Q. Wang, W. Li, I. Hung, F. Mentink-Vigier, X. Wang, G. Qi, X. Wang, Z. Gan, J. Xu, F. Deng, Mapping the oxygen structure of γ-Al_2O_3 by high-field solid-state NMR spectroscopy, Nat. Commun. 11 (2020) 3620.

[71] Z. Zhao, D. Xiao, K. Chen, R. Wang, L. Liang, Z. Liu, I. Hung, Z. Gan, G. Hou, Nature of five-coordinated Al in γ-Al_2O_3 revealed by ultra-high-field solid-state NMR, ACS Cent. Sci. 8 (2022) 795–803.

[72] L. Shen, Y. Wang, J. Du, K. Chen, Z. Lin, Y. Wen, I. Hung, Z. Gan, L. Peng, Probing interactions of γ-Alumina with water via multinuclear solid-state NMR spectroscopy, ChemCatChem 12 (2020) 1569–1574.

[73] C.-H. Chen, E. Gaillard, F. Mentink-Vigier, K. Chen, Z. Gan, P. Gaveau, B. Rebière, R. Berthelot, P. Florian, C. Bonhomme, M.E. Smith, T.-X. Métro, B. Alonso, D. Laurencin, Direct ^{17}O Isotopic Libeling ol Oxides Usiog Mechunochemistry, Inorg. Chem. 59 (2020) 13050–13066.

[74] L. Corti, I. Hung, A. Venkatesh, P.L. Gor'kov, Z. Gan, J.B. Claridge, M. J. Rosseinsky, F. Blanc, Local structure in disordered melilite revealed by ultrahigh field ^{71}Ga and ^{139}La Solid-State Nuclear Magnesolid-sonancn Spectrmscopy, CremPhysChes 25 (2024) e202300934.

[75] A.F. Harper, S.P. Emge, P.C.M.M. Magusin, C.P. Grey, A.J. Morris, Modelling amorphous materials *via* a joint solid-state NMR and X-ray absorption spectroscopy and DFT approach: application to alumina, Chem. Sci. 14 (2023) 1155–1167.

[76] A.R. Haworth, B.I.J. Johnston, L. Wheatcroft, S.L. McKinney, N. Tapia-Ruiz, S. G. Booth, A.J. Nedoma, S.A. Cussen, J.M. Griffin, Structural insight into protective alumina coatings for layered Li-Ion cathode materials by solid-state NMR spectroscopy, ACS Appl. Mater. Interfaces 16 (2024) 7171–7181.

[77] A.J.D. Pauletto, R.J. Bragg, R.I. Walton, M.A. Hope, Resolving ^{209}Bi sites in mixed-halide double perovskites at 28 T, Solid State Nucl. Magn. Reson. 141 (2026) 102052.

[78] D.M. Halat, H. Liu, K. Kim, G.C. Alexander, X. Wang, A. Venkatesh, A.R. Altenhof, H.E. Mason, S.H. Lapidus, J.S. Yoon, Mg-Ion conduction in antiperovskite solid electrolytes revealed by ^{25}Mg Ultrahigh uield NMR fnd First-Prinfirst-pCalculatiocs, J. Am. Chem. Soc. 147 (2025) 27949–27961.

[79] R. Swanson, J. Stebbins, T. Yeo, Y. Xu, I. Hung, Z. Gan, S. McCormack, S. Sen, Structure and fragility of normal and invert lanthanum borate glasses: results from ^{11}B and ^{17}O NMR spectroscopy and calorimetry, J. Non-Cryst. Solids 603 (2023) 122119.

[80] S. Sen, J.F. Stebbins, S. Kroeker, I. Hung, Z. Gan, Evidence for mixed Mg coordination environments in silicate glasses: results from ^{25}Mg NMR Spectroscosy at 35.2 T, J. Phys. Chem. B 127 (2023) 10659–10666.

[81] L. Sánchez-Muñoz, P. Florian, Z. Gan, F. Muñoz, Order–disorder diversity of the solid state by NMR: the role of electrical charges, Minerals 12 (2022) 1375.

[82] L. Corti, I. Hung, A. Venkatesh, Z. Gan, J.B. Claridge, M.J. Rosseinsky, F. Blanc, Cation distribution and anion transport in the $La_3Ga_{5-x}Ge_{1+x}O_{14+0.5x}$Langasite structure, J. Am. Chem. Soc. 146 (2024) 14022–14035.

[83] R.W. Dorn, M.C. Cendejas, K. Chen, I. Hung, N.R. Altvater, W.P. McDermott, Z. Gan, I. Hermans, A.J. Rossini, Structure determination of boron-based oxidative dehydrogenation heterogeneous catalysts with ultrahigh field 35.2 T ^{11}B solid-state NMR spectroscopy, ACS Catal. 10 (2020) 13852–13866.

[84] Z.J. Berkson, S. Björgvinsdóttir, A. Yakimov, D. Gioffrè, M.D. Korzyński, A. B. Barnes, C. Copéret, Solid-state NMR spectra of protons and quadrupolar nuclei at 28.2 T: resolving signatures of surface sites with fast magic angle spinning, JACS Au 2 (2022) 2460–2465.

[85] R.W. Dorn, L.O. Mark, I. Hung, M.C. Cendejas, Y. Xu, P.L. Gor'kov, W. Mao, F. Ibrahim, Z. Gan, I. Hermans, An atomistic picture of boron oxide catalysts for oxidative dehydrogenation revealed by ultrahigh field ^{11}B–^{17}O Solid-Statsolid-spectroscosy, J. Am. Chem. Soc. 144 (2022) 18766–18771.

[86] A. Abragam, The Principles of Nuclear Magnetism, Oxford university press, 1961.

[87] K.J. MacKenzie, M.E. Smith, Multinuclear solid-state Nuclear Magnetic Resonance of Inorganic Materials, Elsevier, 2002.

[88] D.I. Hoult, R.E. Richards, The signal-to-noise ratio of the nuclear magnetic resonance experiment, J. Magn. Reson. 1969 24 (1976) 71–85.

[89] M.J. Duer, Solid State NMR Spectroscopy: Principles and Applications, John Wiley & Sons, 2008.

[90] A. Bhattacharya, Chemistry: breaking the billion-hertz barrier, Nature 463 (2010) 605–606.

[91] K. Hashi, S. Ohki, S. Matsumoto, G. Nishijima, A. Goto, K. Deguchi, K. Yamada, T. Noguchi, S. Sakai, M. Takahashi, Achievement of 1020 MHz NMR, J. Magn. Reson. 256 (2015) 30–33.

[92] E. Luchinat, L. Barbieri, M. Cremonini, L. Banci, Protein in-cell NMR spectroscopy at 1.2 GHz, J. Biomol. NMR 75 (2021) 97–107.

[93] L. Banci, L. Barbieri, V. Calderone, F. Cantini, L. Cerofolini, S. Ciofi-Baffoni, I. C. Felli, M. Fragai, M. Lelli, C. Luchinat, Biomolecular NMR at 1.2 GHz, 2019. ArXiv Prepr. ArXiv191007462.

[94] Bruker Announces First-of-a-kind 1.3 GHz High-Resolution NMR System, (n.d.). https://ir.bruker.com/press-releases/press-release-details/2025/Bruker-Announces-First-of-a-kind-1-3-GHz-High-Resolution-NMR-System/default.aspx.

[95] I. Hung, A.R. Altenhof, R.W. Schurko, D.L. Bryce, O.H. Han, Z. Gan, Field-stepped ultra-wideline NMR at up to 36 T: on the inequivalence between field and frequency stepping, Magn. Reson. Chem. 59 (2021) 951–960.

[96] E.R. Andrew, A. Bradbury, R.G. Eades, Nuclear magnetic resonance spectra from a crystal rotated at high speed, Nature 182 (1958), 1659–1659.

[97] Y. Nishiyama, G. Hou, V. Agarwal, Y. Su, A. Ramamoorthy, Ultrafast magic angle spinning solid-state NMR spectroscopy: advances in methodology and applications, Chem. Rev. 123 (2023) 918–988.

[98] S. Penzel, A. Oss, M.-L. Org, A. Samoson, A. Böckmann, M. Ernst, B.H. Meier, Spinning faster: protein NMR at MAS frequencies up to 126 kHz, J. Biomol. NMR 73 (2019) 19–29.

[99] M. Callon, D. Luder, A.A. Malär, T. Wiegand, V. Římal, L. Lecoq, A. Böckmann, A. Samoson, B.H. Meier, High and fast: NMR protein–proton side-chain assignments at 160 kHz and 1.2 GHz, Chem. Sci. 14 (2023) 10824–10834.

[100] M. Schledorn, A.A. Malär, A. Torosyan, S. Penzel, D. Klose, A. Oss, M.-L. Org, S. Wang, L. Lecoq, R. Cadalbert, Others, protein NMR spectroscopy at 150 kHz magic-angle spinning continues to improve resolution and mass sensitivity, Chembiochem 21 (2020) 2540–2548.

[101] Y. Nishiyama, Y. Endo, T. Nemoto, H. Utsumi, K. Yamauchi, K. Hioka, T. Asakura, Very fast magic angle spinning ^{1}H-^{14}N 2D solid-state NMR: Sub-micro-liter sample data collection in a few minutes, J. Magn. Reson. 208 (2011) 44–48, https://doi.org/10.1016/j.jmr.2010.10.001.

[102] B.P. Tatman, H. Modha, S.P. Brown, Comparison of methods for ^{14}N-^{1}H recoupling in ^{14}N-^{1}H HMQC MAS NMR, J. Magn. Reson. 352 (2023) 107459.

[103] B. Hu, Q. Wang, O. Lafon, J. Trébosc, F. Deng, J.P. Amoureux, Robust and efficient spin-locked symmetry-based double-quantum homonuclear dipolar recoupling for probing ^{1}H–^{1}H proximity in the solid-state, J. Magn. Reson. 198 (2009) 41–48.

[104] D. Massiot, F. Fayon, B. Alonso, J. Trebosc, J.-P. Amoureux, Chemical bonding differences evidenced from J-coupling in solid state NMR experiments involving quadrupolar nuclei, J. Magn. Reson. 164 (2003) 160–164.

[105] G. Tricot, J. Trébosc, F. Pourpoint, R. Gauvin, L. Delevoye, The D-HMQC MAS-NMR technique, in: Annu. Rep. NMR Spectrosc., Elsevier, 2014, pp. 145–184.

[106] C.P. Grey, A.J. Vega, Determination of the Quadrupole coupling constant of the invisible aluminum spins in zeolite HY with ^{1}H/^{27}Al TRAPDOR NMR, J. Am. Chem. Soc. 117 (1995) 8232–8242.

[107] T. Gullion, J. Schaefer, Rotational-echo double-resonance NMR, J. Magn. Reson. 1969 81 (1989) 196–200.

[108] E. Hughes, T. Gullion, A. Goldbourt, S. Vega, A.J. Vega, Internuclear distance determination of S=1, I=1/2 spin pairs using REAPDOR NMR, J. Magn. Reson. 156 (2002) 230–241.

[109] Z. Gan, Measuring multiple carbon–nitrogen distances in natural abundant solids using R-RESPDOR NMR, Chem. Commun. (2006) 4712–4714.

[110] A. Medek, J.S. Harwood, L. Frydman, Multiple-quantum magic-angle spinning NMR: a new method for the study of quadrupolar nuclei in solids, J. Am. Chem. Soc. 117 (1995) 12779–12787.

[111] G. De Paëpe, Dipolar recoupling in magic angle spinning solid-state nuclear magnetic resonance, Annu. Rev. Phys. Chem. 63 (2012) 661–684.

[112] M. Feike, D.E. Demco, R. Graf, J. Gottwald, S. Hafner, H.W. Spiess, Broadband multiple-quantum NMR spectroscopy, J. Magn. Reson. 122 (1996) 214–221.

[113] D.E. Demco, S. Hafner, H.W. Spiess, Rotation-synchronized homonuclear dipolar decoupling, J. Magn. Reson. 116 (1995) 36–45.

[114] M.H. Levitt, Symmetry-based pulse sequences in magic-angle spinning solid-state NMR, in: eMagRes, John Wiley & Sons, Ltd, 2007, https://doi.org/10.1002/9780470034590.emrstm0551.

[115] M. Hohwy, H.J. Jakobsen, M. Edén, M.H. Levitt, N.C. Nielsen, Broadband dipolar recoupling in the nuclear magnetic resonance of rotating solids: a compensated C7 pulse sequence, J. Chem. Phys. 108 (1998) 2686–2694.

[116] A. Brinkmann, M. Edén, M.H. Levitt, Synchronous helical pulse sequences in magic-angle spinning nuclear magnetic resonance: double quantum recoupling of multiple-spin systems, J. Chem. Phys. 112 (2000) 8539–8554.

[117] Q. Wang, B. Hu, O. Lafon, J. Trébosc, F. Deng, J.P. Amoureux, Double-quantum homonuclear NMR correlation spectroscopy of quadrupolar nuclei subjected to

magic-angle spinning and high magnetic field, J. Magn. Reson. 200 (2009) 251–260.
[118] G. Mali, G. Fink, F. Taulelle, Double-quantum homonuclear correlation magic angle sample spinning nuclear magnetic resonance spectroscopy of dipolar-coupled quadrupolar nuclei, J. Chem. Phys. 120 (2004) 2835–2845.
[119] C. Martineau-Corcos, J. Dědeček, F. Taulelle, ^{27}Al-^{27}Al double-quantum single-quantum MAS NMR: applications to the structural characterization of microporous materials, Solid State Nucl. Magn. Reson. 84 (2017) 65–72.
[120] J.-P. Amoureux, C. Fernandez, S. Steuernagel, Z-Filtering in MQMAS NMR, J. Magn. Reson. 123 (1996) 116–118.
[121] D. Massiot, B. Touzo, D. Trumeau, J.P. Coutures, J. Virlet, P. Florian, P. J. Grandinetti, Two-dimensional magic-angle spinning isotropic reconstruction sequences for quadrupolar nuclei, Solid State Nucl. Magn. Reson. 6 (1996) 73–83.
[122] I. Hung, Z. Gan, Isotropic solid-state MQMAS NMR spectra for large quadrupolar interactions using satellite-transition selective inversion pulses and low rf fields, J. Magn. Reson. 324 (2021) 106913.
[123] A. Brinkmann, A.P.M. Kentgens, Proton-selective ^{17}O–H Distance Mdasuremenms in Fast MagicfAnglmagic-angle-slid-Statsolid-spectroscosy for the Determinatdon of Hydrogen Bhnd Lengtbs, Jl Am. Chem. Soc. 128 (2006) 14758–14759.
[124] J.P. Amoureux, J. Trébosc, L. Delevoye, O. Lafon, B. Hu, Q. Wang, Correlation NMR spectroscopy involving quadrupolar nuclei, Solid State Nucl. Magn. Reson. 35 (2009) 12–18.
[125] Z. Gan, ^{13}C/^{14}N heteronuclear multiple-quantum correlation with rotary resonance and REDOR dipolar recoupling, J. Magn. Reson. 184 (2007) 39–43.
[126] J. Trebosc, B. Hu, J.P. Amoureux, Z. Gan, Through-space R^3-HETCOR experiments between spin-1/2 and half-integer quadrupolar nuclei in solid-state NMR, J. Magn. Reson. 186 (2007) 220–227.
[127] A.J. Vega, MAS NMR spin locking of half-integer quadrupolar nuclei, J. Magn. Reson. 1969 96 (1992) 50–68.
[128] M.H. Levitt, Symmetry in the design of NMR multiple-pulse sequences, J. Chem. Phys. 128 (2008) 052205.
[129] B. Hu, J. Trébosc, J.P. Amoureux, Comparison of several hetero-nuclear dipolar recoupling NMR methods to be used in MAS HMQC/HSQC, J. Magn. Reson. 192 (2008) 112–122.
[130] R. Fu, S.A. Smith, G. Bodenhausen, Recoupling of heteronuclear dipolar interactions in solid state magic-angle spinning NMR by simultaneous frequency and amplitude modulation, Chem. Phys. Lett. 272 (1997) 361–369.
[131] F. Pourpoint, Y. Morin, R.M. Gauvin, J. Trébosc, F. Capet, O. Lafon, J.-P. Amoureux, Advances in structural studies on alkylaluminum species in the solid state via challenging ^{27}Al–^{13}C NMR Spectroscosy and X-ray Diffractiod, J. Phys. Chem. C 117 (2013) 18091–18099.
[132] O. Lafon, Q. Wang, B. Hu, F. Vasconcelos, J. Trébosc, S. Cristol, F. Deng, J.-P. Amoureux, Indirect detection via Spin-1/2 nuclei in solid state NMR spectroscopy: application to the observation of proximities between protons and quadrupolar nuclei, J. Phys. Chem. A 113 (2009) 12864–12878.
[133] A. Venkatesh, X. Luan, F.A. Perras, I. Hung, W. Huang, A.J. Rossini, t_1 -Noise eliminated dipolar heteronuclear multiple-quantum coherence solid-state NMR spectroscopy, Phys. Chem. Chem. Phys. 22 (2020) 20815–20828.
[134] I. Hung, Z. Gan, High-Resolution^{1}H/^{17}O NMR Correlatioc under Fast MagicfAnglmagic-aing: sevisitingrCross-Polacross-pn for Quadrupolaq Nuclei, J. nPhys. Chem. Lett. 16 (2025) 7036–7041.
[135] S. Xin, Q. Wang, J. Xu, N. Feng, W. Li, F. Deng, Heteronuclear correlation experiments of ^{23}Na-^{27}Al in rotating solids, Solid State Nucl. Magn. Reson. 84 (2017) 103–110.
[136] B. Fan, W. Zhang, P. Gao, G. Hou, R. Liu, S. Xu, Y. Wei, Z. Liu, Quantitatively mapping the distribution of intrinsic acid sites in mordenite zeolite by high-field ^{23}Na solid-state nuclear magnetic resonance, J. Phys. Chem. Lett. 13 (2022) 5186–5194.
[137] M. Zheng, S. Xin, Q. Wang, J. Trébosc, J. Xu, G. Qi, N. Feng, O. Lafon, F. Deng, Through-space ^{11}B–^{27}Al correlation: Influence if the recoupling channel, Magn. Reson. Chem. 59 (2021) 1062–1076.
[138] R.W. Dorn, A.L. Paterson, I. Hung, P.L. Gor'kov, A.J. Thompson, A.D. Sadow, Z. Gan, A.J. Rossini, Dipolar heteronuclear correlation solid-state NMR experiments between half-integer quadrupolar nuclei: the case of ^{11}B–^{17}O, J. Phys. Chem. C 126 (2022) 11652–11666.
[139] D. Iuga, C. Morais, Z. Gan, D.R. Neuville, L. Cormier, D. Massiot, NMR heteronuclear correlation between quadrupolar nuclei in solids, J. Am. Chem. Soc. 127 (2005) 11540–11541.
[140] R.W. Schurko, Ultra-wideline solid-state NMR spectroscopy, Acc. Chem. Res. 46 (2013) 1985–1995.
[141] A.R. Altenhof, M.J. Jaroszewicz, A.W. Lindquist, L.D.D. Foster, S.L. Veinberg, R. W. Schurko, Practical aspects of recording ultra-wideline NMR patterns under magic-angle spinning conditions, J. Phys. Chem. C 124 (2020) 14730–14744.
[142] T. Wolf, Y. Goobes, L. Frydman, Sensitivity enhancement of ultra-wideline NMR by progressive saturation of the proton reservoir under magic-angle spinning, ChemPhysChem 25 (2024) e202400613.
[143] D. Massiot, I. Farnan, N. Gautier, D. Trumeau, A. Trokiner, J.P. Coutures, ^{71}Ga and ^{69}Ga nuclear magnetic resonance study of β-Ga2O3: resolution of four- and six-fold coordinated Ga sites in static conditions, Solid State Nucl. Magn. Reson. 4 (1995) 241–248.
[144] E.L. Hahn, Spin echoes, Phys. Rev. 80 (1950) 580.
[145] F.H. Larsen, H.J. Jakobsen, P.D. Ellis, N.Chr Nielsen, Sensitivity-enhanced quadrupolar-echo NMR of half-integer quadrupolar nuclei. Magnitudes and relative orientation of chemical shielding and quadrupolar coupling tensors, J. Phys. Chem. A 101 (1997) 8597–8606.
[146] I. Hung, Z. Gan, On the practical aspects of recording wideline QCPMG NMR spectra, J. Magn. Reson. 204 (2010) 256–265.
[147] F.H. Larsen, H.J. Jakobsen, P.D. Ellis, N.Chr Nielsen, QCPMG-MAS NMR of half-integer quadrupolar nuclei, J. Magn. Reson. 131 (1998) 144–147.
[148] L.A. O'Dell, The WURST kind of pulses in solid-state NMR, Solid State Nucl. Magn. Reson. 55–56 (2013) 28–41.
[149] L.A. O'Dell, A.J. Rossini, R.W. Schurko, Acquisition of ultra-wideline NMR spectra from quadrupolar nuclei by frequency stepped WURST–QCPMG, Chem. Phys. Lett. 468 (2009) 330–335.
[150] L.A. O'Dell, Ultra-wideline solid-state NMR: developments and applications of the WCPMG experiment, in: Mod. Magn. Reson., Springer, 2018, pp. 1161–1182.
[151] A.W. MacGregor, L.A. O'Dell, R.W. Schurko, New methods for the acquisition of ultra-wideline solid-state NMR spectra of spin-1/2 nuclides, J. Magn. Reson. 208 (2011) 103–113.
[152] Z. Gan, I. Hung, Second-order phase correction of NMR spectra acquired using linear frequency-sweeps, Magn. Reson. Lett. 2 (2022) 1–8.
[153] J. Koppe, J.E. Frerichs, M.R. Hansen, Pushing the detection limit of static wideline NMR spectroscopy using ultrafast frequency-swept pulses, J. Phys. Chem. Lett. 14 (2023) 10748–10753.
[154] O. Pecher, D.M. Halat, J. Lee, Z. Liu, K.J. Griffith, M. Braun, C.P. Grey, Enhanced efficiency of solid-state NMR investigations of energy materials using an external automatic tuning/matching (eATM) robot, J. Magn. Reson. 275 (2017) 127–136.
[155] I. Hung, K. Shetty, P.D. Ellis, W.W. Brey, Z. Gan, High-field QCPMG NMR of large quadrupolar patterns using resistive magnets, Solid State Nucl. Magn. Reson. 36 (2009) 159–163.
[156] Y. Huang, J. Xu, F. Gul-E-Noor, P. He, Metal-organic frameworks: NMR studies of quadrupolar nuclei, in: Encycl. Inorg. Bioinorg. Chem., John Wiley & Sons, Ltd, 2014, pp. 1–14.
[157] Y. Ma, W. Tong, H. Zhou, S.L. Suib, A review of zeolite-like porous materials, Microporous Mesoporous Mater. 37 (2000) 243–252.
[158] C. Wang, J. Xu, F. Deng, Intermolecular interactions in zeolite catalysis: insights from solid-state NMR spectroscopy, Acc. Chem. Res. 58 (2025) 3328–3340.
[159] P. Pyykkö, Year-2008 nuclear quadrupole moments, Mol. Phys. 106 (2008) 1965–1974.
[160] P. Pyykkö, Year-2017 nuclear quadrupole moments, Mol. Phys. 116 (2018) 1328–1338.
[161] K. Chen, Z. Gan, S. Horstmeier, J.L. White, Distribution of aluminum species in zeolite catalysts: ^{27}Al NMR of aramework,fPartially-partially-c Framework,fand Non-Framewnon-foieties, m. Am. Chem. Soc. 143 (2021) 6669–6680.
[162] M. Ravi, V.L. Sushkevich, J.A. van Bokhoven, Towards a better understanding of Lewis acidic aluminium in zeolites, Nat. Mater. 19 (2020) 1047–1056.
[163] K. Chen, S. Horstmeier, VyT. Nguyen, B. Wang, S.P. Crossley, T. Pham, Z. Gan, I. Hung, J.L. White, Structure and catalytic characterization of a second framework Al(IV) site in zeolite catalysts revealed by NMR at 35.2 T, J. Am. Chem. Soc. 142 (2020) 7514–7523.
[164] N. Thomas, J. Dhainaut, A. Moissette, O. Lafon, G.N. Manjunatha Reddy, Resolving transformative reactions in zeolites under catalytic hydrothermal conditions, J. Phys. Chem. C 128 (2024) 10428–10439.
[165] Z. Qie, J. Hurd, N. Linares, X. Ou, A. Alhelali, Y. Al-Lami, H. Alhassawi, H. Xiang, R. Zou, W.T. Franks, Correlating structural variation with catalytic performance of hierarchical zeolites using ultra-high-field solid-state NMR, ChemCatChem (2025) e00629.
[166] C. Schroeder, J.S. Gómez, A.P.M. Kentgens, L.B. McCusker, C. Baerlocher, C. Dejoie, C.M. Lew, C.-Y. Chen, S.I. Zones, H. Windeck, J. Sauer, M.R. Hansen, H. Koller, Preferred Al locations in the framework structure of the zeolite SSZ-82, Cryst. Growth Des. 25 (2025) 1190–1201.
[167] S.E. Ashbrook, Z.H. Davis, R.E. Morris, C.M. Rice, ^{17}O NMR spectroscopy of crystalline microporous materials, Chem. Sci. 12 (2021) 5016–5036.
[168] C.M. Rice, O.J. Dovernor, R.E. Morris, S.E. Ashbrook, Investigations of the ADOR process using solid-state NMR spectroscopy, Cryst. Growth Des. 23 (2023) 8991–9000.
[169] W. Gao, G. Qi, Q. Wang, W. Wang, S. Li, I. Hung, Z. Gan, J. Xu, F. Deng, Dual active sites on Molybdenum/ZSM-5 catalyst for methane dehydroaromatization: insights from solid-state NMR spectroscopy, Angew. Chem. 133 (2021) 10804–10810.
[170] R.K. Harris, E.D. Becker, S.M. Cabral de Menezes, R. Goodfellow, P. Granger, NMR nomenclature. Nuclear spin properties and conventions for chemical shifts (IUPAC recommendations 2001), Pure Appl. Chem. 73 (2001) 1795–1818.
[171] T.J. Bastow, ^{95}Mo NMR: hyperfine interactions in MoO_3, MoS_2, $MoSe_2$ Mo_3Se_4, $MoSi_2$ and Mo_2C, Solid State Nucl. Magn. Reson. 12 (1998) 191–199.
[172] M.Y. Masoomi, A. Morsali, A. Dhakshinamoorthy, H. Garcia, Mixed-metal MOFs: unique opportunities in metal–organic framework (MOF) functionality and design, Angew. Chem. 131 (2019) 15330–15347.
[173] D. Laurencin, C. Gervais, H. Stork, S. Krämer, D. Massiot, F. Fayon, ^{25}Mg solid-state NMR of magnesium phosphates: high magnetic field experiments and density functional theory calculations, J. Phys. Chem. C 116 (2012) 19984–19995.
[174] I.L. Moudrakovski, R. Alizadeh, J.J. Beaudoin, Natural abundance high field ^{43}Ca solid state NMR in cement science, Phys. Chem. Chem. Phys. 12 (2010) 6961.
[175] C. Bonhomme, X. Wang, I. Hung, Z. Gan, C. Gervais, C. Sassoye, J. Rimsza, J. Du, M.E. Smith, J.V. Hanna, Pushing the limits of sensitivity and resolution for natural abundance ^{43}Ca NMR using ultra-high magnetic field (35.2 T), Chem. Commun. 54 (2018) 9591–9594.
[176] K.M.N. Burgess, Y. Xu, M.C. Leclerc, D.L. Bryce, Alkaline-earth metal carboxylates characterized by^{43}Ca and^{87}Sr solid-state NMR: impact of metal-amine bonding, Inorg. Chem. 53 (2014) 552–561.

[177] L. Lätsch, C.J. Kaul, A.V. Yakimov, I.B. Müller, A. Hassan, B. Perrone, S. Aghazada, Z.J. Berkson, T. De Baerdemaeker, A.-N. Parvulescu, K. Seidel, J. H. Teles, C. Copéret, NMR signatures and electronic structure of Ti sites in Titanosilicalite-1 from solid-state $^{47/49}$Ti NMR Spectroscopy, J. Am. Chems Soc. 145 (2023) 15018–15023.

[178] C. Kaul, J. Koppe, L. Lätsch, M. Wörle, S. Aghazada, J. Holmes, C. Wartmann, M. Zheng, A. Berkessel, T. De Baerdemaeker, Speciation, structural refinement, and distribution of Ti sites in titanium Silicalite-1 from $^{47/49}$Ti NMR Crystallography at 28.2 Tcsla, 2025, https://doi.org/10.26434/chemrxiv-2025-c765h-v3.

[179] K.J. Ooms, V.V. Terskikh, R.E. Wasylishen, Ultrahigh-field solid-state ^{59}Co NMR Studies ofsCo($C_2B_9H_{11}$)$_2$ and Co(C_5H_5)$_2^+$ Salts, J. sm. Chem. Soc. 129 (2007) 6704–6705.

[180] K.M.N. Burgess, C.M. Widdifield, Y. Xu, C. Leroy, D.L. Bryce, Structural insights from ^{59}Co Solid-Statsolid-sxperimente on Organocobalt(I) Catalysts, ChemPhysChem 19 (2018) 227–236.

[181] M. Avramovska, D. Freude, J. Haase, A.V. Toktarev, S.S. Arzumanov, A. A. Gabrienko, A.G. Stepanov, Quantitative ^{67}Zn,^{27}Al and ^{1}H MAS NMR spectroscopy for the characterization of Zn species in ZSM-5 catalysts, Phys. Chem. Chem. Phys. 25 (2023) 28043–28051.

[182] V.K. Michaelis, S. Kroeker, ^{73}Ge solid-state NMR of germanium oxide materials: experimental and theoretical studies, J. Phys. Chem. C 114 (2010) 21736–21744.

[183] M.A. Hanson, A. Sutrisno, V.V. Terskikh, K.M. Baines, Y. Huang, Solid-State^{73}Ge NMR spectroscopy of simple organogermanes, Chem. Eur J. 18 (2012) 13770–13779.

[184] C. Bonhomme, C. Gervais, N. Folliet, F. Pourpoint, C. Coelho Diogo, J. Lao, E. Jallot, J. Lacroix, J.-M. Nedelec, D. Iuga, J.V. Hanna, M.E. Smith, Y. Xiang, J. Du, D. Laurencin, ^{87}Sr solid-state NMR as a structurally sensitive tool for the investigation of materials: antiosteoporotic pharmaceuticals and bioactive glasses, J. Am. Chem. Soc. 134 (2012) 12611–12628.

[185] A.J. Rossini, I. Hung, S.A. Johnson, C. Slebodnick, M. Mensch, P.A. Deck, R. W. Schurko, Solid-state ^{91}Zr NMR Spectroscosy Studies ofsZirconocenz Olefin Polymerizapion Catalyst Pcecursors, J. Am. Chem. Soc. 132 (2010) 18301–18317.

[186] J. Czernek, L. Kobera, L. Havlák, V. Czerneková, J. Rohlíček, J. Bárta, J. Brus, Probing the ^{91}Zr NMR parameters in the solid state by a combination of DFT calculations and experiments, Chem. Phys. Lett. 738 (2020) 136855.

[187] W. Zhang, B.E. Lucier, V. Martins, T. Azizivahed, I. Hung, Y. Xu, Z. Gan, A. Venkatesh, T.W. Goh, W. Huang, Local order, disorder, and everything in between: using ^{91}Zr solid-state NMR spectroscopy to probe zirconium-based metal–organic frameworks, Phys. Chem. Chem. Phys. 27 (2025) 4704–4716.

[188] A. Nadol, F. Venel, R. Giovine, M. Leloire, C. Volkringer, T. Loiseau, C. Gervais, C. Mellot-Draznieks, B. Doumert, J. Trébosc, O. Lafon, F. Pourpoint, Probing the water adsorption and stability under steam flow of Zr-based metal–organic frameworks using ^{91}Zr solid-state NMR spectroscopy, Chem. Sci. 16 (2025) 69–82.

[189] J.V. Hanna, K.J. Pike, T. Charpentier, T.F. Kemp, M.E. Smith, B.E.G. Lucier, R. W. Schurko, L.S. Cahill, A ^{93}Nb Solid-Statsolid-snd Density FudctionalfTheory Stuty of Four- and fix-Coordisix-cNiobate Syntems, Chem. Eur J. 16 (2010) 3222–3239.

[190] O.B. Lapina, D.F. Khabibulin, A.A. Shubin, V.V. Terskikh, Practical aspects of ^{51}V and ^{93}Nb solid-state NMR spectroscopy and applications to oxide materials, Prog. Nucl. Magn. Reson. Spectrosc. 53 (2008) 128–191.

[191] S. Sen, I. Hung, J.M. Lovi, Z. Gan, Application of high-resolution ^{95}Mo Solid Stats NMR spectroscosy in StructuralsStudies ofsComplex Alcali Molabdate mrystals acd Glasses, Jg Phys. Chem. C 129 (2025) 6869–6881.

[192] J.Z. Hu, J.H. Kwak, Y. Wang, C.H.F. Peden, H. Zheng, D. Ma, X. Bao, Studies of the active sites for methane dehydroaromatization using ultrahigh-field solid-state ^{95}Mo NMR Spectroscosy, J. Phys. Chem. C 113 (2009) 2936–2942.

[193] M. Haouas, J. Trébosc, C. Roch-Marchal, E. Cadot, F. Taulelle, C. Martineau-Corcos, High-field ^{95}Mo and ^{183}W static and MAS NMR study of polyoxometalates, Magn. Reson. Chem. 55 (2017) 902–908.

[194] J.J. Kimball, R.W. Schurko, Acquisition of ^{1}H-Detected ^{103}Rh and ^{99}Ru Solid-State Nuclear Magnetic Rsolid-se Spentra in mtationarr Samples, J. Phys. Csem. Lett. s6 (2025) 4596–4601.

[195] K.J. Griffith, F. Ding, S. Flynn, Solid-state nuclear magnetic resonance of spin-9/2 nuclei ^{115}In and ^{209}Bi in functional inorganic complex oxides, Magn. Reson. Chem. 59 (2021) 1077–1088.

[196] F. Chen, G. Ma, G.M. Bernard, R.G. Cavell, R. McDonald, M.J. Ferguson, R. E. Wasylishen, Solid-state ^{115}In and ^{31}P NMR Studies of Triarylphosphine Indium Ttihalide Adducts, J. Am. Chem. Soca 132 (2010) 5479–5493.

[197] A. Sutrisno, C. Lu, R.H. Lipson, Y. Huang, Combined $^{135/137}$Ba Solid-State NMR at an Ultrahigh Magsolid-sield and Compututional Stmdy of β-farium Borcte, J. Phys. Chem. C 113 (2009) 21196–21201.

[198] L.A. O'Dell, I.L. Moudrakovski, A combined ultra-wideline solid-state NMR and DFT study of ^{137}Ba electric field gradient tensors in barium compounds, Chem. Phys. Lett. 565 (2013) 56–60.

[199] C.M. Widdifield, A.D. Bain, D.L. Bryce, Definitive solid-state $^{185/187}$Re NMR spectral evidence for and analysis of the origin of high-order quadrupole-induced effects for I = 5/2, Phys. Chem. Chem. Phys. 13 (2011) 12413.

[200] B. Nowak, D. Kaczorowski, ^{209}Bi NMR in topologically trivial and nontrivial half-heusler bismuthides, J. Phys. Chem. C 120 (2016) 21797–21801.

[201] Z.J. Berkson, M. Bernhardt, C. Copéret, Solid-State ^{183}W NMR Spectroscopy assa High-Resolutionhigh-r of Polyoxptungstatp Structures and synamics, J. Phds. Chem. Lett. 15 (2024) 1950–1955.

[202] M. Berglund, M.E. Wieser, Isotopic compositions of the elements 2009 (IUPAC Technical report), Pure Appl. Chem. 83 (2011) 397–410.

[203] W. Zhang, A. Hassan, J. Struppe, M. Monette, I. Hung, Z. Gan, V. Martins, V. Terskikh, Y. Huang, Overcoming challenges in ^{67}Zn NMR: a new strategy of signal enhancement for MOF characterization, Chem. Commun. 59 (2023) 5205–5208.

[204] S. Yuan, J.-S. Qin, C.T. Lollar, H.-C. Zhou, Stable metal–organic frameworks with group 4 metals: current status and trends, ACS Cent. Sci. 4 (2018) 440–450.

[205] A. Santiago Portillo, H.G. Baldoví, M.T. Garcia Fernandez, S. Navalón, P. Atienzar, B. Ferrer, M. Alvaro, H. Garcia, Z. Li, Ti as mediator in the photoinduced electron transfer of mixed-metal NH2–UiO-66 (Zr/Ti): transient absorption spectroscopy study and application in photovoltaic cell, J. Phys. Chem. C 121 (2017) 7015–7024.

[206] A. Wang, Y. Zhou, Z. Wang, M. Chen, L. Sun, X. Liu, Titanium incorporated with UiO-66 (Zr)-type Metal–Organic Framework (MOF) for photocatalytic application, RSC Adv. 6 (2016) 3671–3679.

[207] B.E. Lucier, Y. Huang, Reviewing $^{47/49}$Ti Solid-State NMR Spectroscsolid-som Alloyssand Simple Cofpounas to Catalssts anc Porous Matecials, in: Annp. Rep. mNMR Spectrosc., Elsevier, 2016, pp. 1–78.

[208] P.H.M. Andrade, A. Nadol, F. Pourpoint, A. Rankin, C. Volkringer, T. Loiseau, M. Hureau, A. Moissette, Structural and electronic insights into titanium-modified UiO-66: probing cation substitution via multi-technique characterization and high-field (1.2 GHz) NMR, J. Phys. Chem. C 130 (2026) 1757–1771.

[209] P. He, B.E. Lucier, V.V. Terskikh, Q. Shi, J. Dong, Y. Chu, A. Zheng, A. Sutrisno, Y. Huang, Spies within metal-organic frameworks: investigating metal centers using solid-state NMR, J. Phys. Chem. C 118 (2014) 23728–23744.

[210] H. Hamaed, M.W. Laschuk, V.V. Terskikh, R.W. Schurko, Application of solid-state ^{209}Bi NMR to the Structural Charscterizatioc of Bismuth-Containbismuth-cials, J. Am. Chem. Soc. 131 (2009) 8271–8279.

[211] W. Zhang, Y. Xu, A. Venkatesh, I. Hung, S. Li, Z. Gan, Y. Huang, Pushing limits of ultra-wideline solid-state NMR spectroscopy: NMR signatures of ^{209}Bi and ^{127}I in Metal–Organic Frameworks at Ulmetal–oh Magnefic Fields, J.uAm. Chem. moc. 147 (2025) 10823–10828.

[212] A.A. Babaryk, O.R. Contreras Almengor, M. Cabrero-Antonino, S. Navalón, H. García, P. Horcajada, A semiconducting $Bi_2O_2(C_4O_4)$ coordination polymer showing a photoelectric response, Inorg. Chem. 59 (2020) 3406–3416.

[213] Z.H. Davis, R.E. Morris, S.E. Ashbrook, Exploring cation distribution in ion-exchanged Al, Ga-containing metal–organic frameworks using ^{17}O NMR spectroscopy, Phys. Chem. Chem. Phys. 25 (2023) 20267–20280.

[214] E.A.L. Borthwick, Z.H. Davis, S.E. Ashbrook, A multinuclear approach to characterising disordered (Al,Sc)-MIL-53 using solid-state NMR spectroscopy, Microporous Mesoporous Mater. 399 (2026) 113868.

[215] V. Martins, B.E.G. Lucier, K. Chen, I. Hung, Z. Gan, C. Gervais, C. Bonhomme, H.-Y. Nie, W. Zhang, Y. Huang, Molecular-level characterization of oxygen local environments in a pristine and post-synthetically modified metal–organic framework via ^{17}O Nuclear Mannetic Rmsonance rpectroscosy, Chem. Mater. 35 (2023) 3555–3569.

[216] V. Martins, J. Xu, I. Hung, Z. Gan, C. Gervais, C. Bonhomme, Y. Huang, ^{17}O solid-state NMR at ultrahigh magnetic field of 35.2 T: resolution of inequivalent oxygen sites in different phases of MOF MIL-53 (Al), Magn. Reson. Chem. 59 (2021) 940–950.

[217] V. Martins, J. Xu, X. Wang, K. Chen, I. Hung, Z. Gan, C. Gervais, C. Bonhomme, S. Jiang, A. Zheng, Higher magnetic fields, finer MOF structural information: ^{17}O solid-state NMR at 35.2 T, J. Am. Chem. Soc. 142 (2020) 14877–14889.

[218] X.-X. Li, S.-T. Zheng, Three-dimensional metal-halide open frameworks, Coord. Chem. Rev. 430 (2021) 213663.

[219] D. Sarkar, A. Bacon, G.M. Bernard, V.K. Michaelis, Metal Halide Perovskite and perovskite-inspired Materials: Solid-State NMR of Quadrupolar Nuclei, 2025.

[220] J.F. Stebbins, L.-S. Du, Chloride ion sites in silicate and aluminosilicate glasses: a preliminary study by ^{35}Cl solid-state NMR, Am. Mineral. 87 (2002) 359–363.

[221] D.L. Bryce, G.D. Sward, Solid-state NMR spectroscopy of the quadrupolar halogens: chlorine-35/37, bromine-79/81, and iodine-127, Magn. Reson. Chem. 44 (2006) 409–450.

[222] B.J. Butler, J.M. Hook, J.B. Harper, Recent advances in the NMR spectroscopy of chlorine, bromine and iodine, Annu. Rep. NMR Spectrosc. 73 (2011) 63–82.

[223] D. Shi, R. Zheng, M. Sun, X. Cao, C. Sun, C. Cui, C. Liu, J. Zhao, M. Du, Semiconductive Copper(I)–Organic frameworks for efficient light-driven hydrogen generation without additional photosensitizers and cocatalysts, Angew. Chem. 129 (2017) 14829–14833.

[224] J. Xu, V.V. Terskikh, Y. Chu, A. Zheng, Y. Huang, ^{13}C chemical shift tensors in MOF α -$Mg_3(HCOO)_6$: which component is more sensitive to host-guest interaction? Magn. Reson. Chem. 58 (2020) 1082–1090.

[225] Y. Li, W. Zhang, Y. Huang, Two open metal sites on the same metal: dynamics of CO_2 in MOF UTSA-74, Magn. Reson. Lett. 1 (2021) 121–130.

[226] A.H. Berge, S.M. Pugh, M.I. Short, C. Kaur, Z. Lu, J.-H. Lee, C.J. Pickard, A. Sayari, A.C. Forse, Revealing carbon capture chemistry with 17-oxygen NMR spectroscopy, Nat. Commun. 13 (2022) 7763.

[227] B.J. Rhodes, L.L. Schaaf, M.E. Zick, S.M. Pugh, J.S. Hilliard, S. Sharma, C. R. Wade, P.J. Milner, G. Csányi, A.C. Forse, ^{17}O NMR spectroscopy reveals CO_2 speciation and dynamics in hydroxide-based carbon capture materials, ChemPhysChem 26 (2025) e202400941.

[228] B.J. Rhodes, J.S. Gomez, J.S. Hilliard, L.L. Schaaf, C.R. Wade, A.C. Forse, ^{17}O-^{1}H correlation NMR spectroscopy provides accessible and direct insights into CO_2 capture chemistry, ChemRxiv 2026 (2026), https://doi.org/10.26434/chemrxiv-2026-kd8l2.

[229] Z. Wang, A.M. Sheveleva, D. Lee, Y. Chen, D. Iuga, W.T. Franks, Y. Ma, J. Li, L. Li, Y. Cheng, Modulation of uptake and reactivity of nitrogen dioxide in metal-organic framework materials, Angew. Chem. 135 (2023) e202302602.